Research Square

Preprints are preliminary reports that have not undergone peer review.
They should not be considered conclusive, used to inform clinical practice,
or referenced by the media as validated information.

Circulation-organized Eurasian heatwaves persist across divergent warming pathways

Yang Gao

yanggao@ouc.edu.cn

Ocean University of China https://orcid.org/0000-0001-6444-6544

Xiaojie Guo

Ocean University of China https://orcid.org/0009-0007-4793-6315

Dehai Luo

Institute of Atmospheric Physics,Chinese Academy of Sciences

Wenju Cai

Ocean University of China https://orcid.org/0000-0001-6520-0829

Tim Woollings

University of Oxford https://orcid.org/0000-0002-5815-9079

Deliang Chen

Tsinghua University https://orcid.org/0000-0003-0288-5618

L. Ruby Leung

Pacific Northwest National Laboratory https://orcid.org/0000-0002-3221-9467

Erich Fischer

ETH Zurich https://orcid.org/0000-0003-1931-6737

Jakob Zscheischler

Helmholtz Centre for Environmental Research https://orcid.org/0000-0001-6045-1629

Emanuele Bevacqua

Helmholtz Centre for Environmental Research-UFZ https://orcid.org/0000-0003-0472-5183

Jian Lu

Ocean University of China

Ke Fan

Sun Yat-Sen University

Zhenzhong Zeng

Southern University of Science and Technology https://orcid.org/0000-0001-6851-2756

Jianqi Sun

National Climate Centre, China Meteorological Administration, Beijing, China.

Xueshun Shen

China Meteorological Administration

Hengyu Zhang

Ocean University of China
Te Yin
Ocean University of China
Xiuwen Guo
Ocean University of China
Wenbin Kou
Ocean University of China
Shaoqing Zhang
Ocean University of China https://orcid.org/0000-0001-6569-9842
Jianping Li
Frontiers Science Center for Deep Ocean Multispheres and Earth System (FDOMES)/Key Laboratory of Physical Oceanography/Institute for Advanced Ocean Studies, Ocean University of China
https://orcid.org/0000-0003-0625-1575
Guangxing Lin
Xiamen University
Huiwang Gao
Ocean University of China https://orcid.org/0000-0002-4274-0811
Lixin Wu
Ocean University of China https://orcid.org/0000-0002-4694-5531

Physical Sciences - Article

Keywords:

Posted Date: November 26th, 2026

DOI: https://doi.org/10.21203/rs.3.rs-10949215/v1

License: This work is licensed under a Creative Commons Attribution 4.0 International License.
Read Full License

Additional Declarations: There is **NO** Competing Interest.

Circulation-organized Eurasian heatwaves persist across divergent warming pathways

Xiaojie Guo[1], Yang Gao[1]*, Dehai Luo[2], Wenju Cai[3,4,5], Tim Woolings[6], Deliang Chen[7,8], L. Ruby Leung[9], Erich Fischer[10], Jakob Zscheischler[11], Emanuele Bevacqua[11], Jian Lu[12], Ke Fan[13], Zhenzhong Zeng[14], Jianqi Sun[15], Xueshun Shen[16], Hengyu Zhang[1], Te Yin[1], Xiuwen Guo[7], Wenbin Kou[1], Shaoqing Zhang[17], Jianping Li[17], Guangxing Lin[5], Huiwang Gao[1] and Lixin Wu[3]

[1]Frontiers Science Center for Deep Ocean Multispheres and Earth System (FDOMES) and Key Laboratory of Marine Environmental Science and Ecology, Ministry of Education, Ocean University of China, Qingdao, 266100, China

[2]State Key Laboratory of Earth System Numerical Modelling and Application, Institute of Atmospheric Physics, Chinese Academy of Sciences, and University of Chinese Academy of Sciences, Beijing, China

[3]Frontiers Science Center for Deep Ocean Multispheres and Earth System, and Key Laboratory of Physical Oceanography, Ministry of Education, the College of Oceanic and Atmospheric Sciences, Ocean University of China, and Laoshan Laboratory, Qingdao, 266100, China

[4]State Key Laboratory of Loess and Quaternary Geology, Institute of Earth Environment, Chinese Academy of Sciences, Xi'an, China

[5]State Key Laboratory of Marine Environmental Science & College of Ocean and Earth Sciences, Xiamen University, Xiamen, China

[6]Atmospheric, Oceanic and Planetary Physics, University of Oxford, OX1 3PU, Oxford, UK

[7]Department of Earth System Science, Tsinghua University, Beijing 100084, China

[8]Institute for Carbon Neutrality, Tsinghua University, Beijing 100084, China

[9]Atmospheric, Climate & Earth Sciences Division, Pacific Northwest National Laboratory, Richland, WA, 99352, USA

[10]Institute for Atmospheric and Climate Science, ETH Zurich, Zurich, 8092, Switzerland

[11]Department of Compound Environmental Risks, Helmholtz Centre for Environmental Research – UFZ, 04318 Leipzig, Germany

[12]College of Oceanic and Atmospheric Sciences, Ocean University of China, Qingdao, 266100, China

[13]School of Atmospheric Sciences, Sun Yat-sen University/ Southern Marine Science and Engineering Guangdong Laboratory (Zhuhai), China

[14]State Key Laboratory of Soil Pollution Control and Safety, Southern University of Science and Technology, China

[15]National Climate Center, China Meteorological Administration, Beijing 100081, China

[16]The Center of Earth System Modeling and Prediction, CMA, Beijing, 100081, China

[17]Frontiers Science Center for Deep Ocean Multispheres and Earth System, and Key Laboratory of Physical Oceanography, Ministry of Education, the College of Oceanic and Atmospheric Sciences, Ocean University of China, Qingdao, 266100, China

*Correspondence to: yanggao@ouc.edu.cn

Abstract

Damaging heatwaves are shaped by thermodynamic warming and atmospheric circulation that sometimes organize heat anomalies into persistent, spatially coherent events. Whether mitigation constrains these thermodynamic and circulation-organized dimensions equally remains unclear. Combining reanalysis with high-resolution Earth System Model simulations, we identify a class of spatially organized Eurasian heatwaves that last longer, exhibit twice the spatial co-occurrence, and have 2.5–3.0 °C larger event-mean temperature anomalies than less organized heatwaves. The cumulative heat load of such events has increased nearly five times faster, with a more rapid expansion of simultaneous land exposure. Importantly, across simulated warming pathways, a lower warming, though strongly limits the cumulative heat load, does not produce a commensurate reduction in the organized-heatwave events that are defined relative to their contemporaneous mean climate state. This persistence coincides with broad, occurrence-driven blocking enhancement, indicating that circulation-organized heatwave characteristics respond less strongly to mitigation than their thermodynamic burden.

Recent heat extremes in Europe provide a stark reminder that the most damaging heatwaves are not simply local temperature exceedances. In June 2026, an unusually early and intense heatwave sustained by an omega-block pattern affected much of western and central Europe, bringing widespread record-breaking heat across France, Germany, the United Kingdom, Poland and Spain, with major consequences for health, wildfire risk, power supply and transport infrastructure (Abnett, 2026; Copernicus Climate Change Service, 2026). Such events highlight a broader challenge: high-impact heatwave hazard depends not only on thermodynamic warming, but also on the ability of atmospheric circulation to organize heat anomalies into large, persistent and spatially coherent events (Barriopedro et al., 2023; Domeisen et al., 2023).

Anthropogenic warming has already increased the frequency and intensity of hot extremes over most land regions, and further warming is expected to amplify heatwave hazards (Domeisen et al., 2023; IPCC, 2021). This understanding underpins warming-level risk assessment, in which lower-emission pathways reduce the thermal background and thereby lower the likelihood of exceeding dangerous temperature thresholds. Yet moderate warming does not preclude high-impact climate outcomes. Recent work has shown that sector-relevant extremes at 2 °C warming can exceed multi-model-mean outcomes at 3 °C or 4 °C, underscoring that impact-relevant hazards cannot be inferred from global-mean warming alone (Bevacqua et al., 2026). This distinction is particularly important for heatwaves, whose impacts depend not only on temperature magnitude but also on event-scale properties such as duration, spatial extent, co-occurrence and cumulative heat load. Unlike the thermodynamic background, these properties can depend strongly on atmospheric circulation and spatial organization, whose responses need not scale monotonically with global-mean warming (Barriopedro et al., 2023; Domeisen et al., 2023; Luo et al., 2023; Rogers et al., 2022). It therefore remains unclear how lower-warming pathways alter both the thermodynamic severity and circulation-driven organization that make heatwaves persistent and spatially extensive.

Eurasia provides a particularly important setting in which to examine this distinction. The continent spans densely populated regions, semi-arid interiors and high-latitude ecosystems, so spatially extensive heatwaves can generate cascading impacts across public health, agriculture, energy demand, transport and fire-prone landscapes (Forzieri et al., 2018; Groisman et al., 2018; Gu et al., 2019; Kornhuber et al., 2020; Rogers et al., 2022; Ruffault et al., 2020; Vicedo-Cabrera et al., 2021). Such extremes can also have broader Earth-system consequences, as recent evidence links warm and dry conditions under persistent Siberian high-pressure systems to enhanced fire-related methane emissions (Zhu et al., 2026). Large-scale circulation can organize concurrent and spatially extensive heat extremes through amplified Rossby waves, recurrent wave packets and quasi-stationary anomalies (Fang and Lu, 2024; Kornhuber et al., 2020; Liu et al., 2025; Ma et al., 2024; Rousi et al., 2022; Wang

et al., 2025). Event-based approaches have therefore become increasingly useful for characterizing heatwaves as coherent spatiotemporal systems rather than isolated local exceedances (Lo et al., 2021; Luo et al., 2022, 2024; Rogers et al., 2022). These advances have clarified how large-scale heat extremes are organized, but whether their thermodynamic severity and circulation-related occurrence respond similarly across warming pathways remains unresolved.

Atmospheric blocking provides one of the clearest circulation mechanisms for organizing persistent heat extremes. Blocking anticyclones can enhance subsidence, suppress cloud formation, reduce ventilation and sustain surface warming over large areas (Barriopedro et al., 2023; Kautz et al., 2022; Pfahl and Wernli, 2012; Woollings et al., 2018). Yet the future response of blocking remains difficult to constrain. Climate models have long exhibited biases in blocking frequency, persistence and regional distribution, particularly over the Northern Hemisphere (Davini and D'Andrea, 2016, 2020; Kautz et al., 2022; Schiemann et al., 2020; Wang et al., 2026). Many projections suggest an overall decline in blocking under strong warming, but regional and seasonal responses remain uncertain and can be sensitive to model resolution (Lohmann et al., 2024; Schiemann et al., 2020; Woollings et al., 2018). High-resolution modelling may help reduce some of this uncertainty. A high-resolution Earth system model has been shown to substantially reduce the long-standing underestimation of Northern Hemisphere summer blocking frequency in CMIP6 models and to project a significant late-century increase in summer blocking over northern Russia under high warming, a regional signal not evident in the CMIP6 multi-model mean (Gao et al., 2025). These uncertainties complicate assessment of the dynamical contribution to heatwave changes across warming pathways and motivate the use of high-resolution simulations as a testbed for examining circulation-organized heatwave hazard.

Here we use the ERA5 reanalysis for 1975–2025 to identify Eurasian heatwave events and distinguish a more spatially organized class characterized by greater persistence, intensity and spatial co-occurrence. We quantify historical changes in these characteristics and examine their associated large-scale circulation. We then use the high-resolution Community Earth System Model (CESM-HR) to assess changes in organized heatwaves under low- and high-warming pathways, defining extreme events relative to the contemporaneous climate state of each pathway. We focus on event occurrence, spatial organization, cumulative heat load and atmospheric blocking. By comparing thermal and circulation-related characteristics across pathways, we assess whether reduced warming weakens both the thermodynamic severity and large-scale organization of Eurasian heatwaves. We find that lower warming substantially reduces thermal burden but does not produce a commensurate reduction in organized-heatwave occurrence, coinciding with stronger blocking under the lower-warming pathway.

A distinct class of spatially organized Eurasian heatwaves

Eurasian heatwaves occur across a broad geographical range, from densely populated low- and mid-latitude regions to ecologically vulnerable high latitudes (Extended Data Fig. 1). Based on event duration, spatial co-occurrence and temperature intensity during May–September 1975–2025, we identify two distinct heatwave classes, hereafter referred to as Type A and Type B (Figure 1; see Methods). Type B events are more persistent, spatially extensive and thermally intense than Type A events, with longer durations, approximately twice the mean spatial co-occurrence fraction, and event-mean temperature anomalies that are 2.5–3.0 °C larger (Figure 1a–c). We therefore characterize Type B as a distinct class of spatially organized Eurasian heatwaves, reflecting its greater persistence, spatial co-occurrence and intensity.

These differences translate into a substantially greater cumulative heat burden. Integrating temperature anomaly, event duration and affected area, Type B events produce a much larger annual cumulative heat load, with an absolute increase of 357×10^6 km² °C days per decade compared with 75×10^6 km² °C days per decade for Type A events (Figure 1d). This larger absolute increase partly reflects the higher baseline heat load of Type B events. The fraction of Eurasian land simultaneously affected by Type B heatwaves also shows a larger absolute increase, rising by 1.40 percentage points per decade compared with 0.81 percentage points per decade for Type A events (Fig. 1e). Although the annual occurrence of both event types has increased, the mean spatial extent of individual Type B events has also expanded more strongly in absolute terms (Extended Data Fig. 2a,b). In contrast, historical changes in event duration and maximum temperature anomaly are comparatively modest (Extended Data Fig. 2c,d). Together, these results indicate that the growing absolute burden of Type B heatwaves has been expressed primarily through greater spatial co-occurrence and expansion in affected area, rather than pronounced increases in event duration or peak intensity.

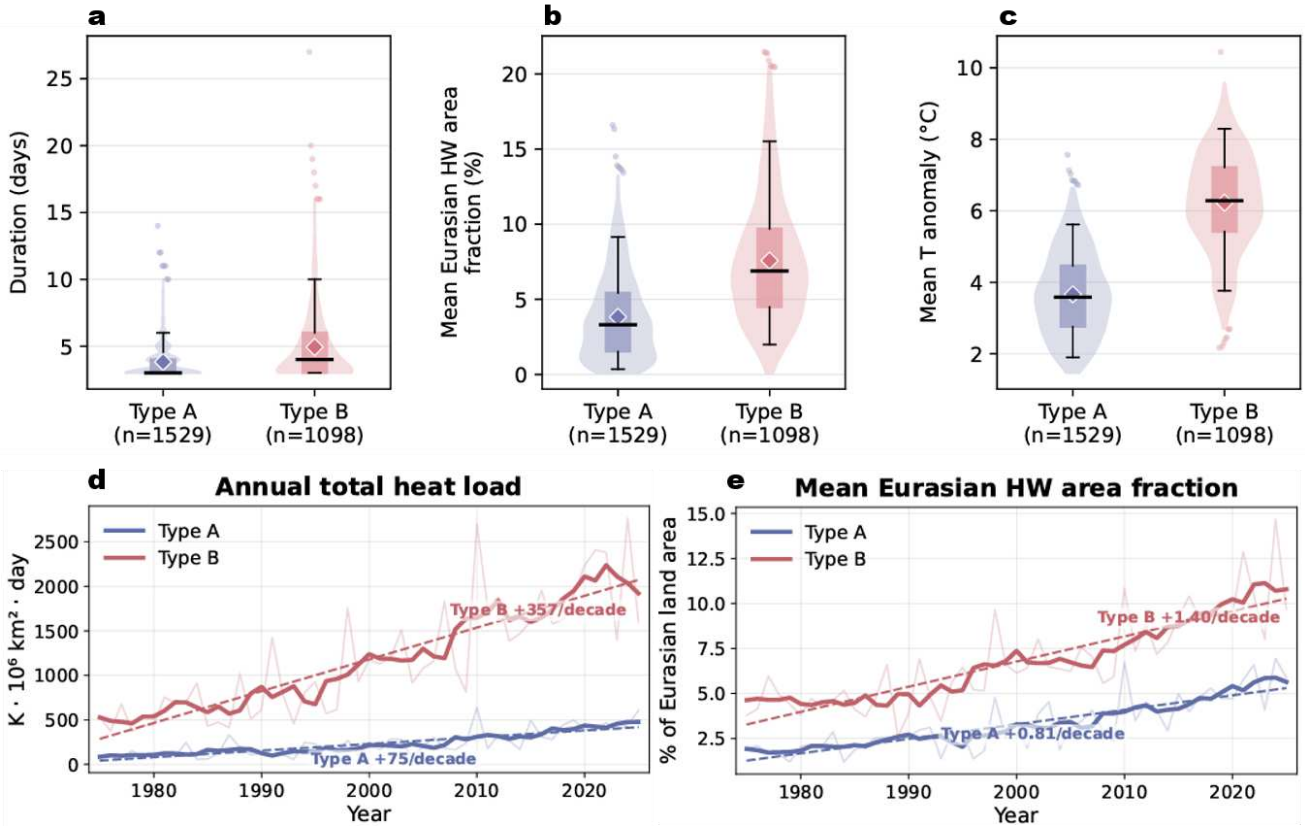

Figure 1 Characteristics and historical changes of two types of Eurasian heatwave events. **a–c,** Distributions of event characteristics for Type A and Type B heatwaves identified over Eurasia during 1975–2025： **a**， event duration; **b,** mean Eurasian heatwave area fraction; and **c,** event-mean temperature anomaly. Violin plots show the distributions, boxplots indicate the interquartile range and median, diamonds denote the mean, and sample sizes are shown below each category. **d,e,** Historical evolution of **d,** annual total heat load and **e,** mean Eurasian heatwave area fraction for Type A and Type B events. Thin lines show annual values, thick lines indicate 5-year centred rolling means, and dashed lines denote ordinary least-squares linear trends; trend magnitudes are labelled for each event type. Heat load is calculated by integrating temperature anomaly over event duration and affected area. For each event, the mean Eurasian heatwave area fraction is the percentage of total Eurasian land area experiencing heatwave conditions, averaged over the event lifetime. Annual values in **e** are calculated by averaging this event-level quantity across all events of the corresponding type in each year.

The spatial distributions and circulation composites further reveal distinct large-scale environments associated with the two event types. Type A events are concentrated mainly over low- and mid-latitude Eurasia (Figure 2a), whereas Type B events occur more extensively across the mid- and high latitudes of Europe, Russia and Siberia, with an additional hotspot over the northern Indian

subcontinent (Figure 2b). Type B events are accompanied by stronger and more spatially coherent positive 500-hPa geopotential-height anomalies, including prominent anomalous high-pressure centres over Europe and the Ural region (Figure 2c,d). Blocking activity also differs markedly around heatwave onset: Type B events exhibit higher blocking probability and larger blocked-area fraction, with blocking progressively strengthening before onset and peaking around day 0, whereas Type A events show little comparable evolution (Figure 2e,f). Sensitivity analyses controlling for event location and coastal proximity, and repeating the classification after removing systematic geographical dependence, confirm that Type B remains more persistent, spatially concurrent and more closely associated with atmospheric blocking (Supplementary Figs. 4–6). Together, these results identify Type B as a distinct, spatially organized class of Eurasian heatwaves closely associated with persistent large-scale blocking, motivating our focus on these events in the subsequent analysis.

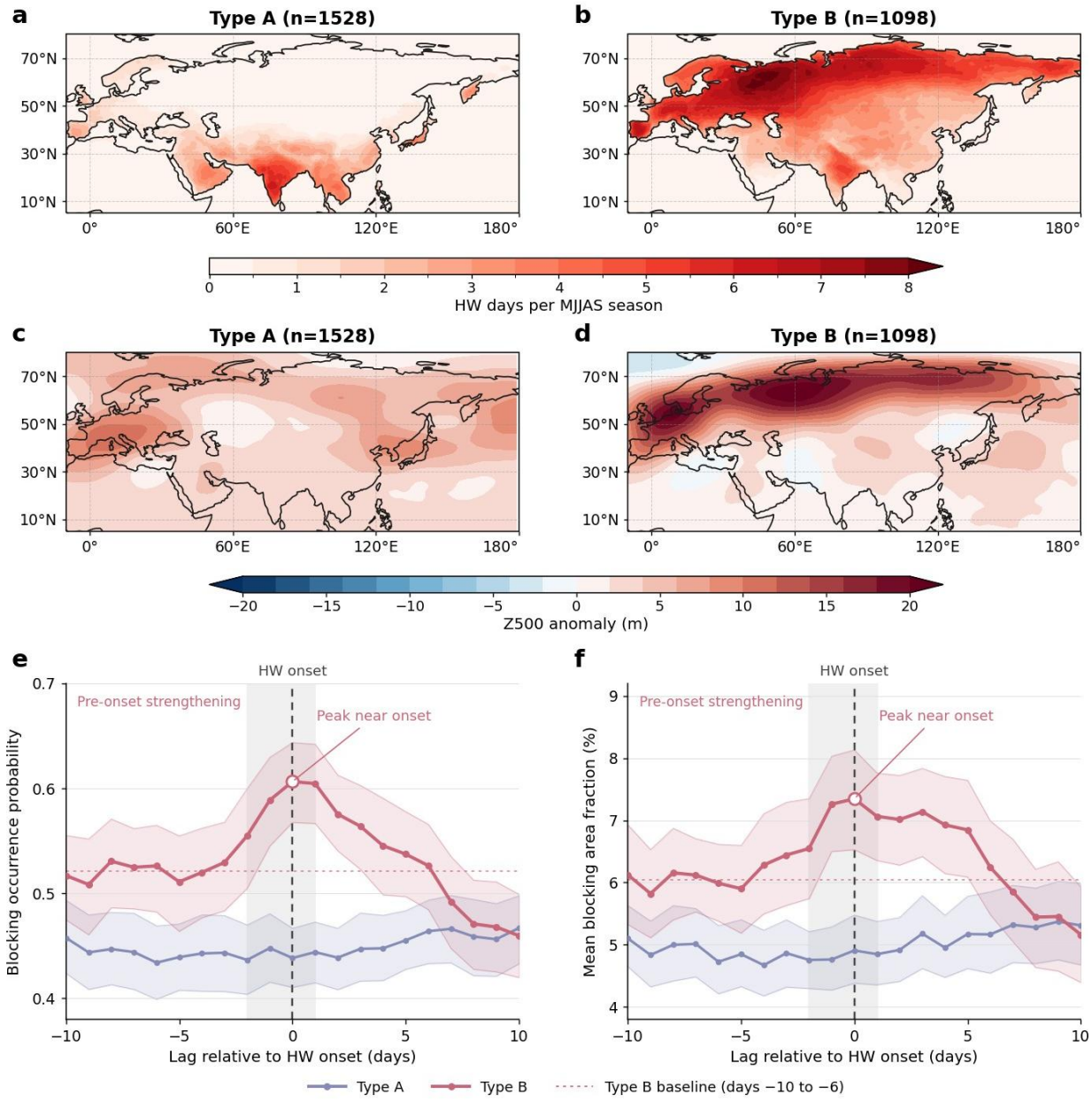

Figure 2 Circulation characteristics and blocking evolution associated with the two classes of Eurasian heatwave events. a,b, Spatial distributions of the mean annual number of May–September (MJJAS) heatwave days associated with **a,** Type A and **b,** Type B events. Values indicate the number of heatwave days per MJJAS season at each grid cell contributed by each event type. **c,d,** Event-composite 500-hPa geopotential height (Z500) anomalies for **c**, Type A and **d**, Type B heatwaves, calculated relative to the 1975–2025 MJJAS climatology. **e,f,** Heatwave-onset-aligned evolution of **e**, blocking occurrence probability and f, mean blocking area fraction from 10 days before to 10 days after heatwave onset (day 0). Lines show event-composite means at each lag, and shading denotes pointwise 95% confidence intervals estimated from 2,000 complete event-onset-year bootstrap resamples. Blocking is identified within the Eurasian blocking domain (10°W–180°E, 40°–75°N)

using the criterion described in Methods. The blocking area fraction is defined as the fraction of the total area of this domain classified as blocked, including both land and ocean grid cells. Insets show event-level blocking metrics calculated over the actual heatwave duration: the fraction of heatwave days coinciding with blocking in the Eurasian blocking domain in **e** and the mean blocking area fraction during the event in **f**. Boxes indicate the interquartile range, black horizontal lines the median, and coloured circles the mean. Inset values differ from the lag composites because they summarize variable-length heatwave periods event by event, whereas each point on the lag curves represents a fixed day relative to onset. The dashed vertical line marks heatwave onset.

Lower warming weakens thermal burden more than organized heatwave occurrence

Organized heatwave occurrence shows substantial overlap between the two warming states despite markedly different levels of thermal burden. To assess changes in organized heatwaves (Type B events) across warming pathways, we used simulations from the high-resolution coupled Earth system model CESM-HR (see Methods). Previous studies have shown that CESM-HR substantially improves the simulation of Northern Hemisphere summer blocking relative to lower-resolution CMIP6 models, particularly by reducing biases in the frequency of long-lasting blocking events (Gao et al., 2025). It also more accurately reproduces the skewness of Northern Hemisphere summer temperature distributions and associated heatwave characteristics relative to the CMIP5 ensemble (Gao et al., 2023). Our evaluation further shows that CESM-HR reproduces the principal contrasts between the two heatwave types in duration, spatial co-occurrence and temperature anomaly, together with the broad spatial distribution of organized heatwaves and their associated positive high-latitude geopotential-height anomalies (Extended Data Fig. 3). These similarities provide a basis for examining future changes in organized heatwaves and their circulation environment with CESM-HR.

By mid-century, organized-heatwave occurrence and thermal burden show contrasting responses across the two warming states. Using period-specific climatologies and percentile thresholds, the primary CESM-HR realization contains 573 organized heatwave events historically, increasing to 657 at GWL 1.5 °C and 611 at GWL 3.0 °C (Figure 3a). The increase is concentrated mainly among events lasting 3–7 days, whereas changes in longer-lasting events are smaller and less monotonic. Across the multi-member ensembles, the exact ordering varies among realizations, but occurrence changes overlap substantially between the two warming states (Extended Data Fig. 8a). Substantially weaker warming at GWL 1.5 °C therefore does not translate into a correspondingly lower occurrence of organized heatwaves when events are defined relative to their contemporaneous climate state.

Thermal burden, by contrast, separates much more clearly between the warming states. Event

heat load increases more strongly at GWL 3.0 °C, with the contrast becoming particularly evident for longer-lasting events (Figure 3b). The multi-member simulations reinforce this separation: member-level occurrence changes overlap substantially between GWL 1.5 °C and GWL 3.0 °C, whereas cumulative event heat load increases much more strongly under the higher-warming pathway (Extended Data Fig. 8a,b). Thus, organized-heatwave occurrence does not scale with warming level as directly as cumulative thermal burden.

Other dimensions of heatwave organization show substantially less separation between the two warming states. Spatial patterns of organized-heatwave occurrence are broadly comparable, with increases and decreases distributed across similar parts of Eurasia despite local differences in magnitude and significance (Figure 3c,d). Mean event duration shows a similarly overlapping regional response (Figure 3e,f), while changes in spatial co-occurrence remain modest across duration classes (Extended Data Fig. 4). Event-mean temperature anomaly and spatial extent show clearer warming-level contrasts, particularly under GWL 3.0 °C, consistent with the stronger increase in cumulative heat load under higher warming (Extended Data Fig. 4). Together, these results indicate substantially less pathway separation in event occurrence, persistence and spatial organization than in thermal burden.

The substantial overlap in occurrence is retained when future events are classified using fixed historical scaling and cluster centroids, although the magnitude and, for some members, the sign of future-minus-historical changes are more sensitive to classifier definition (Supplementary Fig. 1). We therefore interpret the occurrence response primarily in terms of the overlap between warming pathways rather than differences in their ensemble-mean changes.

Overall, lower warming markedly constrains the cumulative thermal burden of organized Eurasian heatwaves without producing a commensurate reduction in their relative occurrence or organization. The thermodynamic and organizational dimensions of heatwave hazard therefore do not respond in parallel across warming pathways, motivating examination of whether contrasting circulation responses help explain this residual organized-heatwave occurrence.

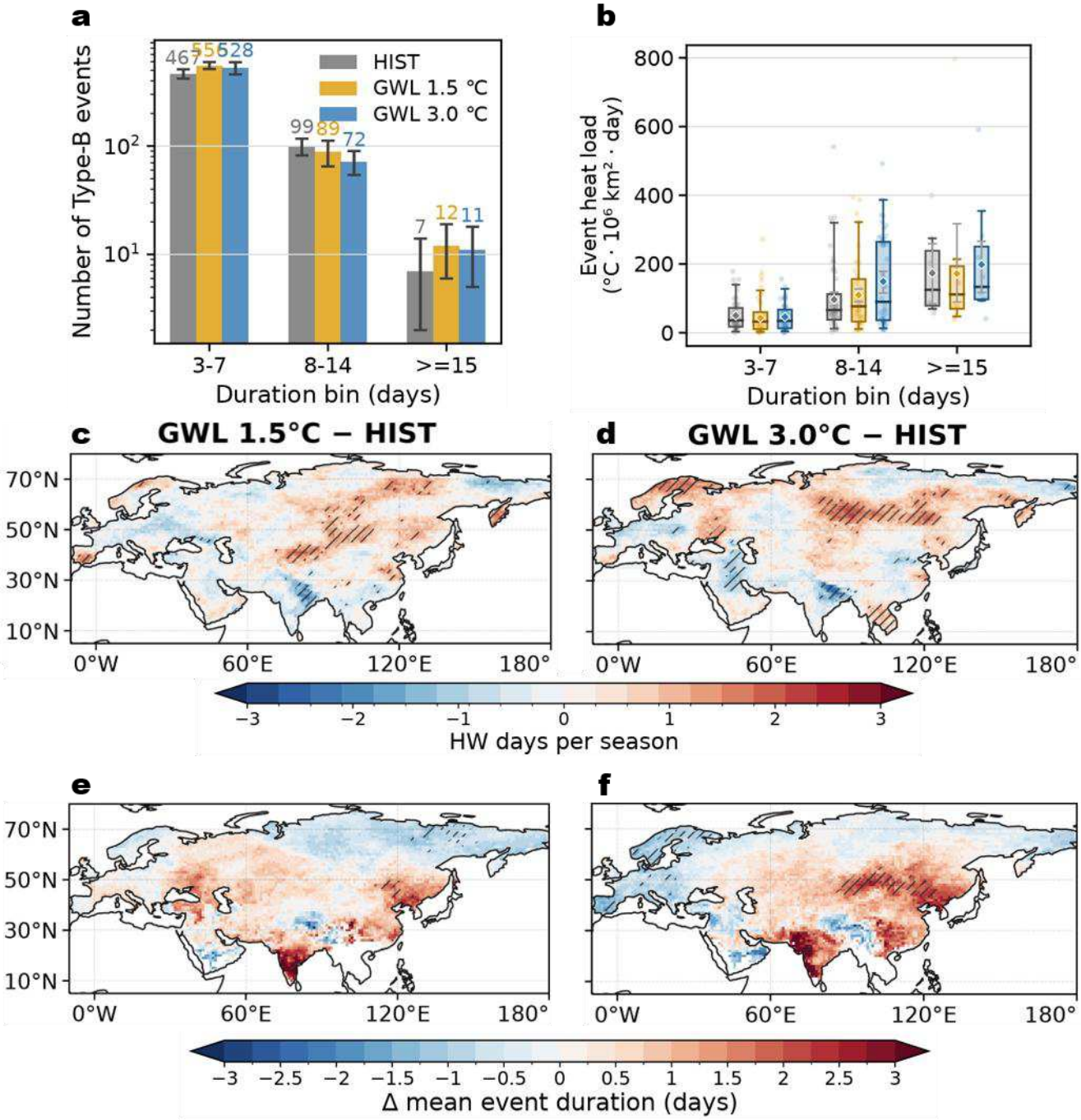

Figure 3. Duration-dependent occurrence, thermal burden and spatial changes of organized Eurasian heatwaves in historical and mid-century simulations. CESM-HR simulations are compared between the historical period (HIST; 1975–2004) and two mid-century warming states corresponding to approximately 1.5 °C and 3.0 °C of global warming above the pre-industrial baseline, represented by 2041–2070 under RCP2.6 and RCP8.5, respectively. **a**, Number of organized heatwave events in three duration classes (3–7, 8–14 and ≥15 days). Numbers above the bars indicate event counts, and error bars show two-sided 95% confidence intervals estimated from 2,000 bootstrap resamples of complete MJJAS years within each 30-year period. **b**, Distributions of cumulative event

heat load for the same duration classes. Boxes indicate the interquartile range, black horizontal lines the median, and whiskers the 5th–95th percentile range; points represent individual events. Diamonds denote the mean, with coloured error bars showing two-sided 95% confidence intervals estimated from 2,000 bootstrap resamples of complete MJJAS years. **c,d**, Future-minus-historical changes in the mean annual number of organized heatwave days per MJJAS season for **c**, GWL 1.5 °C and **d**, GWL 3.0 °C. **e,f**, Corresponding changes in mean event duration for **e**, GWL 1.5 °C and **f**, GWL 3.0 °C. Hatching in **c–f** indicates grid cells where future and historical values differ at the 95% confidence level based on a two-sided Welch's *t*-test ($p \leq 0.05$).

Contrasting dynamical support across warming pathways

Given the close association between organized heatwaves and large-scale blocking in ERA5, together with their correspondence in the historical CESM-HR simulation, we next examined whether contrasting heatwave responses across warming pathways are accompanied by changes in their circulation environment. We considered two complementary aspects: blocking–heatwave coupling and changes in blocking activity itself.

Historically, 51% of organized heatwave days coincide with blocking. This fraction increases significantly to 59% at GWL 1.5 °C, an 8-percentage-point rise, but remains close to its historical value at GWL 3.0 °C (50%; Figure 4a). By contrast, the mean blocked-area fraction on organized heatwave days changes only modestly, from 5% historically to 6% at GWL 1.5 °C and 5% at GWL 3.0 °C, with neither future change statistically significant (Figure 4b). Other coupling diagnostics, including the number of organized heatwave events per blocking event, the probability of an organized heatwave day given a blocking day, and heat load and spatial co-occurrence on blocking days, also show only modest, statistically insignificant changes (Extended Data Fig. 5). The clearest low-warming signal is therefore an increase in the fraction of organized heatwave days occurring under blocked conditions, rather than a uniform strengthening of blocking–heatwave coupling across all metrics.

The spatial relationship between blocking and organized heatwaves also differs between the two pathways. We compared organized-heatwave occurrence and persistence under blocking and non-blocking conditions within each climate state and then evaluated the future-minus-HIST change in this contrast (Figure 4c–f). At GWL 1.5 °C, the blocking-associated occurrence contrast becomes more positive across much of western, southern and eastern Eurasia, despite decreases over parts of central and northern Eurasia. At GWL 3.0 °C, decreases become more widespread across northern Eurasia, particularly high-latitude Siberia, while positive changes are concentrated mainly in the central and eastern mid-latitudes. Persistence shows a broadly similar transition, with increases over much of mid-

latitude Eurasia at GWL 1.5 °C but more extensive decreases across northern and eastern Eurasia at GWL 3.0 °C. These regional redistributions occur despite the absence of a statistically significant change in the domain-mean probability of an organized heatwave day given a blocking day (Extended Data Fig. 5), indicating that changes are expressed more clearly in geographical structure than in domain-mean coupling strength. Other blocking-associated characteristics, including heat load, intensity and spatial co-occurrence, are more spatially heterogeneous and do not show a similarly consistent low-warming enhancement (Extended Data Fig. 6). Across the available members, the fraction of organized heatwave days coinciding with blocking nevertheless tends to increase more at GWL 1.5 °C, although the blocking–heatwave interaction remains spatially and inter-member variable (Extended Data Fig. 8c,d; Supplementary Fig. 2). Together, these results indicate a pathway-dependent reorganization of the blocking–heatwave relationship, but the signal is not uniform across coupling diagnostics or realizations.

A clearer pathway contrast emerges in blocking activity itself (Figure 5). At GWL 1.5 °C, blocking frequency increases across a broad region extending from the North Atlantic and northern Europe through the Barents–Kara sector and eastward across high-latitude Eurasia. The Shapley decomposition attributes most of this enhancement to increased blocking occurrence, whereas changes in mean residence duration are weaker and vary regionally in sign (Figure 5a–c). At GWL 3.0 °C, blocking-frequency changes are more spatially heterogeneous, with decreases across large parts of the Eurasian Arctic and increases confined to several regional centres (Figure 5d). Occurrence contributions are weaker and more fragmented, while residence-duration changes show stronger regional contrasts, yielding a spatial reorganization rather than a broad enhancement of blocking activity (Figure 5e,f).

The available multi-member simulations preserve this difference in the character of the blocking response (Extended Data Fig. 9). The low-warming ensemble exhibits a broad, predominantly occurrence-driven increase in blocking, whereas the high-warming ensemble shows a weaker and more eastward-shifted reorganization, with decreases over the North Atlantic–western Eurasian sector and increases displaced farther east. Considerable member-to-member variability remains, particularly under stronger warming, but substantial portions of these spatial responses recur across realizations (Supplementary Fig. 3). The ensemble evidence therefore supports a pathway-dependent asymmetry in blocking behaviour while emphasizing considerable uncertainty in its regional expression and in the associated blocking–heatwave interaction.

Blocking-onset decomposition provides further insight into this contrast. At GWL 1.5 °C, increases in blocking onset arise primarily from a higher probability of onset when comparable

precursor circulation states occur, rather than from an increased frequency of those precursor states themselves (Figure 5g,h). Although changes in the annual-mean North Atlantic Oscillation (NAO) index are modest, the number of days in its positive phase (NAO+) increases by 7% at GWL 1.5 °C but decreases by 6% at GWL 3.0 °C (Extended Data Fig. 7a). This contrast is consistent with differences in upstream circulation conditions associated with downstream blocking (Luo et al., 2015; Luo et al., 2015; Woollings et al., 2018). Meanwhile, the weaker background meridional potential-vorticity gradient across much of mid- to high-latitude Eurasia at GWL 1.5 °C (Extended Data Fig. 7b) indicates a dynamical environment more favourable for the amplification and persistence of blocking anomalies (Luo et al., 2019, 2025; Luo and Zhang, 2020).

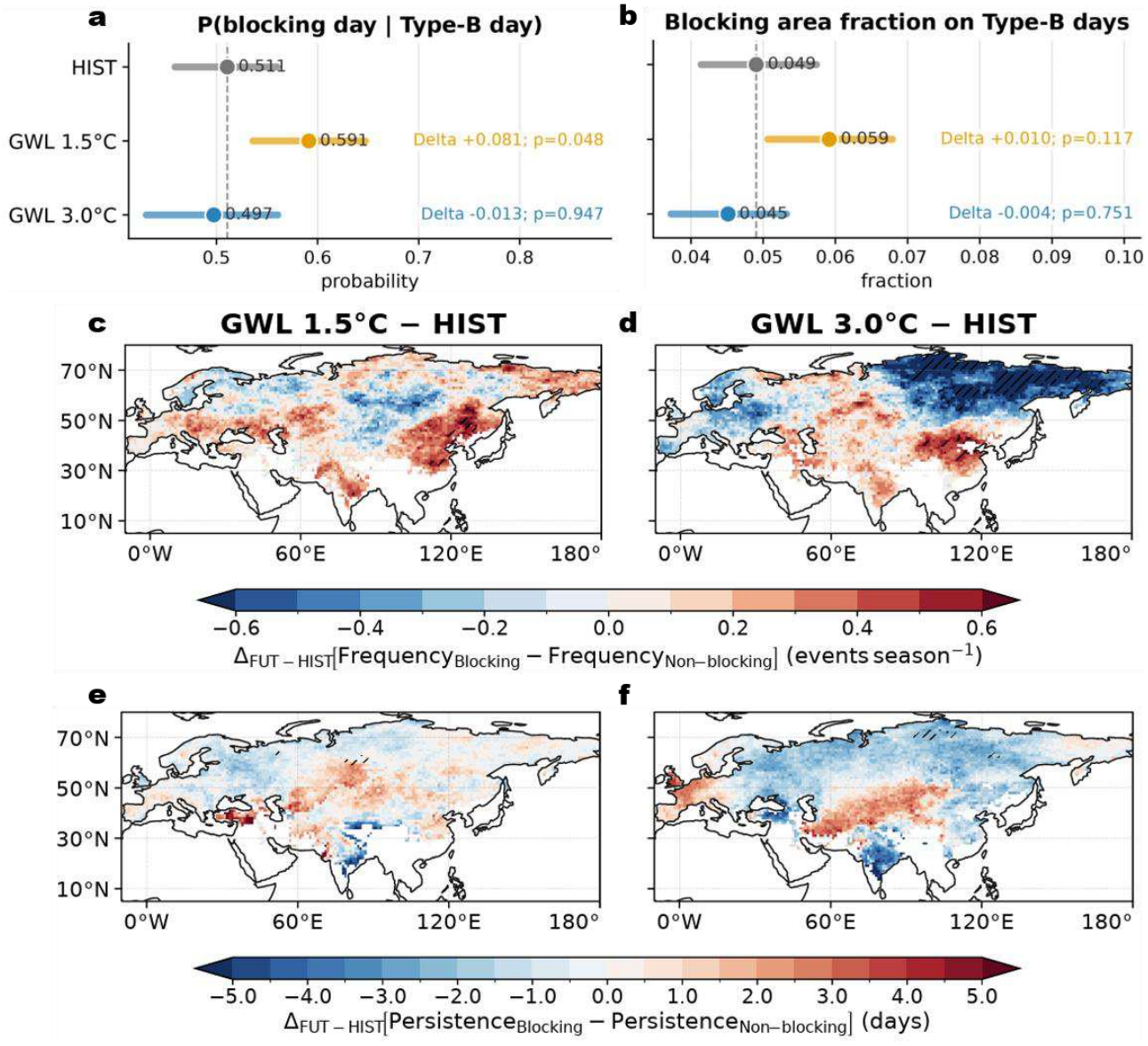

Figure 4 Changes in blocking–organized heatwave coupling and blocking-associated

contrasts in heatwave characteristics across two mid-century warming states. Blocking–organized heatwave relationships are evaluated in CESM-HR for HIST (1975–2004) and two mid-century warming states, GWL 1.5°C and GWL 3.0°C, represented by 2041–2070 under RCP2.6 and RCP8.5, respectively. **a**, Conditional probability that an organized heatwave day coincides with blocking, and **b**, mean blocking area fraction on organized heatwave days. Points show 30-year estimates; horizontal lines show two-sided 95% confidence intervals from 2,000 bootstrap resamples of complete MJJAS years. Dashed lines indicate HIST estimates, and annotations show future-minus-HIST differences and unadjusted P values from two-sided Welch's t-tests of annual values. **c,d**, Future-minus-HIST changes in the strong-blocking versus no-blocking contrast in organized heatwave occurrence frequency for GWL 1.5°C and GWL 3.0°C, respectively. **e,f**, As in **c,d**, but for persistence. Positive values indicate a more positive strong-blocking versus no-blocking contrast in the future. Blank cells denote insufficient samples; hatching indicates $p<0.05$ from two-sided Welch's t-tests of annual contrast values.

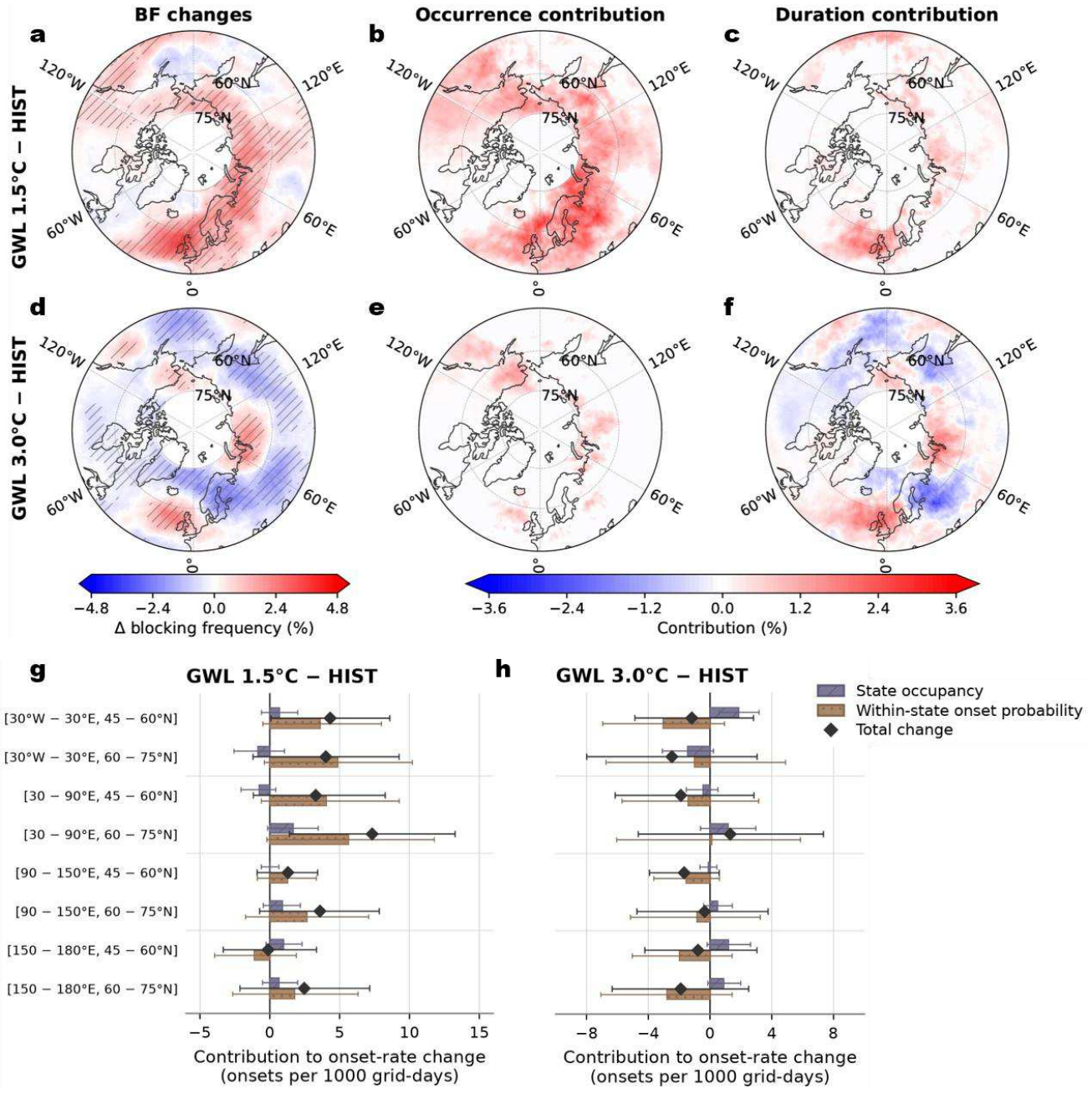

Figure 5 Spatial changes in blocking frequency and decomposition of blocking-onset changes. Future-minus-HIST changes in warm-season blocking are shown for GWL 1.5 °C and GWL 3.0 °C, represented by 2041–2070 under RCP2.6 and RCP8.5, respectively; HIST covers 1975–2004. **a–f,** Changes in May–September (MJJAS) blocking frequency and contributions from local spell occurrence and residence duration. **a–c,** GWL 1.5 °C minus HIST; **d–f,** GWL 3.0 °C minus HIST. Panels **a,d** show total blocking-frequency changes, **b,e** the occurrence contribution and **c,f** the residence-duration contribution, derived using a two-factor midpoint decomposition. Values are expressed in percentage points. Hatching in **a,d** indicates grid cells where annual MJJAS blocking frequencies differ between future and HIST periods ($P \leq 0.05$, two-sided Welch's *t*-test). **g,** Regional

decomposition of blocking-onset-rate changes, complementing the occurrence-related contribution shown in **b,e**. Future-minus-HIST changes in onset rate are separated into state-occupancy and within-state onset-probability contributions for four Eurasian longitude sectors, each divided into 45°–60° N and 60°–75° N bands. Results are shown for GWL 1.5 °C (left) and GWL 3.0 °C (right). Bars show the two contributions and diamonds their sum. Values are blocking onsets per 1,000 grid-days; error bars indicate two-sided 95% confidence intervals from 2,000 bootstrap resamples of complete MJJAS years.

Summary and outlook

Climate mitigation strongly reduces the thermodynamic burden of Eurasian heatwaves, but its effects on their organization are less straightforward. In our simulations, the high-warming pathway produces substantially greater cumulative heat load, whereas organized-heatwave occurrence and spatial organization, defined relative to the contemporaneous climate state of each pathway, show much less separation between the low- and high-warming ensembles. This contrast illustrates that different dimensions of regional heatwave hazard need not scale in parallel with global-mean temperature. Regional responses depend not only on warming magnitude but also on the evolving background climate, forcing composition and internal variability, such that a lower-warming climate is not simply a weakened version of a higher-warming climate (Good et al., 2015; Lehner and Coats, 2021; Maule et al., 2017). Similar non-monotonic behaviour has been documented for other regional responses, including Arctic amplification relative to global-mean warming (Liang et al., 2022; Ono et al., 2022). Our results therefore distinguish a strong mitigation benefit in cumulative thermal burden from a more weakly separated response in the occurrence and large-scale organization of heat extremes.

Atmospheric blocking provides a physically plausible dynamical context for this divergence. Although the simulation and projection of blocking remain uncertain (Davini and D'Andrea, 2020; Lohmann et al., 2024; Schiemann et al., 2020; Woollings et al., 2018), CESM-HR substantially reduces Northern Hemisphere summer blocking biases, particularly for long-lived events (Gao et al., 2025). Across the available simulations, the low-warming pathway tends towards a broad, predominantly occurrence-driven enhancement of blocking, whereas the high-warming pathway shows a weaker and more spatially heterogeneous reorganization, with decreases over the North Atlantic–western Eurasian sector and increases displaced farther east. Blocking support for organized heatwaves also tends to be stronger in the low-warming ensemble, despite substantial regional and member-to-member variability. Blocking-onset decomposition further indicates that this contrast is associated primarily with a higher probability of blocking onset within comparable precursor circulation states rather than with more frequent occurrence of those states. Changes in NAO+ occurrence and the background meridional

potential-vorticity gradient provide additional, physically consistent dynamical context, although their contributions to the ensemble-level contrast are not directly isolated. Spatially heterogeneous circulation responses can moreover be obscured by ensemble or multi-model averaging when their location and magnitude vary among realizations (Shepherd, 2014; Shepherd et al., 2018; Zappa and Shepherd, 2017). Together, these results are consistent with blocking contributing to the persistence and spatial organization of heatwaves under lower warming, without implying that it is the sole dynamical control.

Several caveats limit attribution of this contrast to global warming level itself. The two warming states are sampled from distinct forcing pathways and therefore differ not only in global-mean temperature but also in forcing composition and transient climate evolution. Anthropogenic aerosol emissions and burdens evolve differently between the pathways, and their spatially heterogeneous forcing can modify Eurasian summer temperature and pressure patterns, the strength and position of the westerly jet, North Atlantic–European circulation and Northern Hemisphere summer storm tracks independently of their contribution to global-mean warming (Dong et al., 2022; Undorf et al., 2018). Greenhouse-gas forcing, aerosol evolution, ocean–atmosphere adjustment and internal variability may therefore all contribute to the contrasting blocking responses. Internal variability can remain comparable to forced regional circulation changes on multidecadal timescales (Deser, 2020; Hawkins and Sutton, 2009; Jain et al., 2023; Maher et al., 2020), while the available ensembles differ substantially in size, limiting quantitative comparison of their response distributions. The occurrence result also retains some sensitivity to heatwave classification: substantial overlap between the low- and high-warming ensembles persists when future events are classified using fixed historical scaling and cluster centroids, although the magnitude, and for some realizations the sign, of future-minus-historical changes is more sensitive to classifier definition (Supplementary Fig. 1). Larger and more balanced initial-condition ensembles, multiple high-resolution models, common-GWL experiments across different pathways and single-forcing experiments will be needed to separate these contributions more rigorously. Further investigation of jets, storm tracks, stationary waves, Arctic amplification and ocean–atmosphere coupling could also clarify the transition from broad blocking enhancement in the low-warming simulations to a more eastward-shifted and spatially heterogeneous response under stronger warming (Athanasiadis et al., 2020; Coumou et al., 2018).

Limiting warming remains essential for reducing the absolute intensity and cumulative thermal burden of Eurasian heatwaves. Yet our results show that circulation-organized heatwave occurrence exhibits substantially less separation between lower- and higher-warming pathways than cumulative thermal burden. Stronger blocking support provides a plausible dynamical contribution to this residual occurrence under lower warming, although its magnitude remains pathway- and variability-dependent.

Regional risk assessment should therefore consider not only global-mean warming, but also how forcing pathways shape atmospheric circulation and, in turn, the persistence and spatial organization of extreme heat. This distinction is particularly relevant for adaptation: mitigation strongly constrains the thermodynamic component of heatwave hazard, whereas circulation-organized extremes may respond less monotonically to global-mean warming and therefore require explicit consideration in regional risk assessment.

Overall, the thermodynamic and organizational dimensions of Eurasian heatwave hazard do not respond in parallel across warming pathways. Global-mean warming is therefore an essential but incomplete metric of regional extreme-heat risk.

Data Availability

ERA5 reanalysis data are available from the Copernicus Climate Change Service (https://cds.climate.copernicus.eu). The CESM-HR historical and RCP8.5 simulations used for the primary analyses are publicly available through the International Laboratory for High-Resolution Earth System Prediction (iHESP) at https://ihesp.github.io/ihesp_web/. Additional CESM-HR ensemble simulations are available through the NSF NCAR Geoscience Data Exchange (GDEX). The 10-member MESACLIP historical ensemble (1920–2005) is available at https://gdex.ucar.edu/datasets/d651007/ (Castruccio et al., 2024a), and the corresponding 10-member RCP8.5 ensemble (2006–2100) is available at https://gdex.ucar.edu/datasets/d651009/ (Castruccio et al., 2024b). The CESM-HR RCP2.6 simulation used in this study is part of the iPOGS dataset and is available at https://gdex.ucar.edu/datasets/d651043/ (Castruccio et al., 2025).

Code Availability

The source code of the high-resolution Community Earth System Model (CESM-HR) used in this study is publicly available through the International Laboratory for High-Resolution Earth System Prediction (iHESP) at https://ihesp.github.io/ihesp_web/. Python scripts used for the analyses and figure generation in this study are available from the corresponding author upon reasonable request.

Acknowledgements

This work was supported by the National Natural Science Foundation of China (42375189), the Science and Technology Innovation Project of Laoshan Laboratory (LSKJ202300400,1-4, LSKJ202202201), and the Department of Science and Technology of Shandong Province (2022GJJLJRC02-049). We thank for the technical support of the National Large Scientific and

Technological Infrastructure “Earth System Numerical Simulation Facility” (https://cstr.cn/31134.02.EL). DC was supported by the Carbon Neutrality and Energy System Transformation (CNEST) Program and Tsinghua University (100008001). LRL was supported by the Office of Science, U.S. Department of Energy, Biological and Environmental Research as part of the Earth and Environmental System Modeling program. PNNL is operated for the DOE by Battelle Memorial Institute through Contract DE-AC05-76RL01830.

Author Contributions

Y.G. conceived the study and led the development of the methodology. X.J. Guo developed the study framework, performed the analyses and drafted the manuscript. D.L., T.W., J.L. and K.F. contributed to the interpretation of atmospheric circulation dynamics, particularly the role of changes in atmospheric blocking. W.C., D.C., L.R.L., E.B., Z.Z. contributed to discussions of the manuscript structure and the interpretation of the results. E.F., J.Z., J.S., X.S., H.Z., T.Y., X.W. Guo, W.K., S.Z., J.L., G.L., H.G. and L.W. contributed to the interpretation and discussion of the results. All authors contributed to the writing of the paper.

Competing Interests

The authors declare no competing interests.

Methods

Model descriptions and reanalysis data

We used high-resolution Earth system model simulations spanning 250 years from 1850 to 2100. The experiments followed the Coupled Model Intercomparison Project Phase 5 (CMIP5) protocol (Taylor et al., 2012), using CMIP5 historical forcings through 2005 and the Representative Concentration Pathway 2.6 (RCP2.6; Van Vuuren et al., (2011)) or Representative Concentration Pathway 8.5 (RCP8.5; Riahi et al., (2011)) thereafter. Simulations were performed with the high-resolution configuration of CESM1.3 (Chang et al., 2020). The atmosphere and land components were run at nominal 0.25° horizontal resolution, and the ocean and sea-ice components at nominal 0.1° horizontal resolution. The atmospheric model included several modifications, including changes to the vertical advection scheme, gravity-wave parameterization and dust parameterization. In addition, the dynamical core was switched from the finite-volume core to the spectral-element core to support scalable high-resolution integrations on large numbers of computational cores (Chang et al., 2020; Zhang et al., 2020).

Model analyses were conducted using 30-year time windows: a historical baseline from 1975 to 2004 and a mid-century period from 2041 to 2070. Based on the model-simulated global mean surface temperature evolution relative to the pre-industrial baseline (1850–1900), the primary RCP2.6 and RCP8.5 simulations during 2041–2070 correspond approximately to 1.5 °C and 3 °C global warming levels (GWLs) above the pre-industrial baseline, respectively. To sample internal variability and pathway dependence, additional CESM-HR realizations described by Chang et al., (2026) were included. The GWL 1.5 °C ensemble comprises three realizations, including two RCP2.6 simulations and one simulation following SSP2-com, a reality-aligned combined emissions scenario derived from Shared Socioeconomic Pathway 2 (SSP2) and incorporating updated greenhouse-gas and air-pollutant emissions and national mitigation commitments (Zhong et al., 2025) whereas the GWL 3.0 °C ensemble comprises nine RCP8.5 realizations (members 2–10), together with their corresponding historical members (Chang et al., 2026). Because the scenario forcings start in 2005, the historical baseline period ends before the onset of the scenario integrations. For ensemble-mean blocking diagnostics at GWL 3.0 °C, member 5 was excluded because its blocking-frequency response exerted disproportionate leverage on the ensemble mean. Its Eurasian-domain mean change was −1.40 percentage points, compared with −0.37 to +0.32 percentage points across the other eight realizations, reflecting a much stronger and more spatially coherent decrease (Supplementary Fig. 4). Including this member therefore shifts the ensemble-mean response towards a broad reduction rather than the regionally heterogeneous reorganization evident across most realizations. Member 5 was retained in

member-level analyses of ensemble spread. For consistency in heatwave detection, event tracking, and spatial diagnostics, all model fields used in the analysis were bilinearly interpolated to a common 1° grid and aggregated to daily means where needed before further processing.

We also used ERA5, the fifth-generation atmospheric reanalysis produced by the European Centre for Medium-Range Weather Forecasts (Hersbach et al., 2020), as an observationally constrained reference for heatwave detection and classification. ERA5 fields were analyzed for 1975 to 2025. The original ERA5 data were available at hourly temporal resolution and 0.25° horizontal resolution. For consistency with the model-based analyses and event-tracking framework, the ERA5 fields were bilinearly interpolated to the same common 1° grid and aggregated to daily means before calculating temperature anomalies, heatwave masks, and event-level diagnostics.

Blocking detection and tracking

To minimize uncertainty arising from the choice of blocking index, we employ two representative hybrid blocking metrics. The first method prioritizes a meridional reversal of geopotential-height gradients and additionally imposes a high-pressure structural criterion, whereas the second method prioritizes the high-pressure structure and additionally requires a meridional geopotential-height reversal. Both methods are applied to daily 500 hPa geopotential height fields, and only blockin1g events persisting for at least five consecutive days are retained.

i. Hybrid index 1

The following indices are calculated for each longitude, over latitudes from 40° to 75° N:

$$GHGN(\lambda,\phi) = \frac{Z(\lambda,\phi+\Delta) - Z(\lambda,\phi)}{\Delta} < -10 GHGS(\lambda,\phi) = \frac{Z(\lambda,\phi) - Z(\lambda,\phi-\Delta)}{\Delta} > 0, Z_{anomaly}(\lambda,\phi) =$$

$$Z(\lambda,\phi) - \bar{Z}(\phi) > 0,$$

where GHGN (GHGS) denotes the meridional gradient of 500 hPa geopotential height Z to the north (south); $Z(\lambda,\phi)$is the 500 hPa geopotential height at longitude $\lambda$and latitude ϕ; and $\bar{Z}(\phi)$is the zonal mean of Zat latitude ϕ. Here $\Delta = 15°$. Requiring a positive daily zonal anomaly of Zensures that blocked points are embedded within a high-pressure system, thereby reducing the likelihood of identifying cut-off low (P. Liu et al., 2018).

If the above conditions are satisfied, the grid point is classified as locally blocked. A blocking region is identified when the meridional extent of contiguous blocked points exceeds 15°. For each blocking region, the center is defined as the location of the maximum 500 hPa geopotential height (Z_{500}). Blocking events are then tracked following Masato et al., 2013. For two consecutive days (day

n and day $n+1$), blocking is considered to belong to the same event if the blocking center on day $n+1$ lies within 27° latitude and 36° longitude of the center on day n; otherwise, day $n+1$ is treated as the start of a new event. If multiple blocking centers are detected on day $n+1$, the one closest to the center on day $n$is assigned to the ongoing event. Within a given event, the center on any day is additionally required to remain within 1.5 times the 27° latitude by 36° longitude distance relative to the center on the first day of the event. Finally, only events persisting for at least five days are retained.

ii. Hybrid index 2

This method detects atmospheric blocking from daily 500 hPa geopotential height, $Z(\lambda, \phi, t)$, using a two-step procedure (instantaneous detection followed by duration filtering), largely following the unified eddy–ABS index framework (P. Liu, 2020). First, we compute zonal eddies:

$$Z'(\lambda, \phi, t) = Z(\lambda, \phi, t) - \bar{Z}(\phi, t),$$

where $\bar{Z}(\phi, t)$ is the zonal mean of Z at latitude ϕ. For each day t, a high object is defined as a contiguous region where $Z'(\lambda, \phi, t)$ exceeds a seasonally varying percentile threshold. The threshold is obtained as the 75th percentile of Z' within a 90-day centered window, using values over 40°–80°N. Only objects with area larger than $1.5 \times 10^6\ km^2$ are retained. Each object is represented by its core, defined as the grid point where Z' reaches its local maximum.

For each retained high, we diagnose a Tibaldi–Molteni-type meridional gradient reversal using the absolute geopotential height field Z. Let ϕ_c denote the core latitude and Δ denote a meridional offset (in degrees latitude). The north and south gradients are defined as:

$$GHGN(\lambda, t) = \frac{Z(\lambda, \phi_c + \Delta, t) - Z(\lambda, \phi_c, t)}{\Delta},$$

$$GHGS(\lambda, t) = \frac{Z(\lambda, \phi_c, t) - Z(\lambda, \phi_c - \Delta, t)}{\Delta}.$$

A high is classified as an instantaneous blocking (IB) feature if the gradients satisfy $GHGN(\lambda, t) \leq -10$ and $GHGS(\lambda, t) \geq 0$. To reduce sensitivity to the exact choice of ϕ_c, we allow a small latitude search around the core (±8°) when applying the reversal test. All grid points within the corresponding high object are then labeled as blocked on day t, yielding a daily IB mask.

Persistent blocking (PB) events are subsequently obtained by tracking daily IB objects in time. Two objects on consecutive days are linked if their centers remain quasi-stationary, requiring a small longitudinal displacement (daily speed ≤ 10 °/day) and maximum overlap between adjacent days. Only tracks persisting for at least 5 consecutive days are retained as PB events. Finally, the blocking mask is constructed by retaining only those grid points and days that are involved in the identified PB

events.

iii. Combination

Each hybrid index is converted to a binary daily mask and remapped to a common grid. The final hybrid blocking mask is defined as:

$$B_{final}(\lambda, \phi, t) = B_H1(\lambda, \phi, t) \cup B_H2(\lambda, \phi, t),$$

where B_H1 and B_H2 denote the masks from Hybrid index 1 and Hybrid index 2, respectively. Overlapping detections are counted only once. B_{final} is used for all subsequent frequency, duration, and event-level diagnostics.

Blocking events are re-tracked from B_{final} over 40°–75°N and all longitudes. Daily blocked objects are identified using 8-neighbor connectivity. Objects on days t and $t + 1$ are linked when:

$$|\Delta\phi_c| \leq 27°,$$

$$|\Delta\lambda_c| \leq 36°,$$

$$|\phi_c(t) - \phi_c(t_0)| \leq 1.5 \times 27°,$$

$$|\lambda_c(t) - \lambda_c(t_0)| \leq 1.5 \times 36°,$$

where c denotes the area-weighted centroid and t_0 is the first day of the event. If multiple objects satisfy these criteria, the nearest object to the previous-day centroid is assigned to the ongoing event. Only events lasting at least 5 consecutive days and beginning and ending within MJJAS are retained.

Following Gao et al., (2025), an event is classified as a Eurasian regional blocking event if its start and end centroids both fall within 30°W–180°E and 40°–75°N. Events are also retained when one endpoint centroid is inside this region and the opposite endpoint has longitudinal coverage within the region exceeding half of the regional longitude extent. Because the tracking is applied to a binary mask, event centers are defined by area-weighted centroids rather than maximum-Z500 locations. For each retained event, lifetime, area, area-time integral, displacement, speed, growth and decay timing, growth and decay rates, and shape factor are calculated.

Warm-season blocking frequency decomposition

Warm-season blocking frequency is calculated directly from B_{final} as:

$$BF(\lambda, \phi) = N_{blocked}(\lambda, \phi) \,/\, N_{MJJAS}.$$

Local blocked spells are then identified independently at each grid cell within each MJJAS season.

We define:

$$f = N_{spells}/N_{MJJAS}, D = N_{blocked}/N_{spells}, BF = f \times D.$$

This identity is used only for diagnostic attribution. Future-minus-historical changes are decomposed using a two-factor Shapley decomposition:

$$\Delta BF = C_f + C_D,$$

where C_f and C_D denote the occurrence and residence-duration contributions, respectively. The Shapley method averages the marginal contribution of each factor over the two possible update orders and assigns the interaction term equally to the two factors.

Heatwave detection and tracking

Daily heatwave events were identified from near-surface air-temperature anomalies during May to September (the warm season). For each dataset or scenario, the seasonal-cycle climatology was calculated separately over its corresponding analysis period using a truncated Fourier fit retaining the first two harmonics, corresponding to the annual and semi-annual components of the seasonal cycle. At each grid cell, heatwave days were then defined as days when the anomaly exceeded the local 90th-percentile threshold calculated from May-to-September anomalies within the same dataset or scenario and over the same analysis period. Thus, both the climatology and percentile threshold were specific to each dataset or scenario. This relative-threshold framework largely removes the direct influence of shifts in the mean state of temperature, while retaining differences associated with internal variability, changes in the shape of the temperature distribution, and the temporal evolution of warming within each analysis period. The same dataset- or scenario-specific anomaly field was also used to calculate event-level heatwave intensity, such as temperature anomaly, for the subsequent classification.

The detection was restricted to Northern Hemisphere land. The land mask was applied before thresholding, spatial connectivity, and temporal tracking, so that ocean grid cells did not contribute to heatwave objects or event propagation. Daily heatwave objects were identified from the binary exceedance field using 8-neighbour connectivity. Objects on two consecutive days were linked into the same spatiotemporal event when their intersection-over-union $\geqslant 0.5$. For each tracked event, event duration was defined as the number of consecutive days between its first and last detected occurrence, inclusive. Only events lasting at least 3 consecutive days and reaching a maximum area of at least $1 \times 10^5 km^2$ were retained. The final gridded heatwave mask, event-ID field, and exceedance field were filtered using the same retained event catalogue to ensure consistency between gridded and event-level products.

Definition of Eurasian land heatwave events and classification

Eurasian land heatwave events were selected from the tracked land-only heatwave catalogue within the Eurasian analysis domain, defined as 10°W–180°E and 5°–80°N. To quantify continental-scale co-occurrence, a daily Eurasia-wide heatwave fraction was calculated as:

$$F_{(HW)}(t) = \frac{\left(\sum_i A_i\, L_i HW_i(t)\right)}{\left(\sum_i A_i\, L_i\right)},$$

where A_i is grid-cell area, L_i is land fraction, and $HW_i(t)$ is the binary heatwave mask at grid cell i on day t. The summation was taken over Eurasian land grid cells. For each tracked event, $F_{(HW)}(t)$ was summarized over the event lifetime using its mean, maximum, and 90th percentile values.

Tracked Eurasian heatwave events were classified into two types using k-means clustering with $k = 2$. The clustering was based on three standardized event-level features: event duration, event-mean temperature anomaly, and Eurasia-wide co-occurrence. To avoid classifying events primarily by the long-term warming signal, the co-occurrence metric was detrended before clustering:

$$cofrac_{(resid)} = cofrac_{(mean)} - (a + b \times year),$$

and then year-centered as:

$$cofrac_{(yc)} = cofrac_{(resid)} - median\left(cofrac_{(resid)}\ in\ the\ same\ year\right).$$

The final co-occurrence feature used in clustering was $cofrac_{(yc)}$, which represents the year-centered residual of the event-mean Eurasian heatwave fraction. In contrast, the event-mean intensity was retained in its original temperature anomaly, because a sensitivity test showed that additionally detrending and year-centering this intensity metric had little effect on the resulting two-type classification. Type B was defined as the cluster with the larger summed standardized feature means, corresponding to events with greater persistence, stronger temperature anomalies, and broader Eurasian co-occurrence. Type A denotes the other cluster.

Spatial distributions of Type-B heatwave occurrence, persistence, and intensity

Type-B heatwave occurrence was quantified as the mean number of days per MJJAS season during which each land grid cell was occupied by a tracked Type-B event. A daily binary occupancy indicator, $H_s(x, t)$, was defined as 1 when grid cell x belonged to the footprint of a Type-B event on day t, and 0 otherwise. The climatological number of Type-B heatwave days was calculated as

$$D_s(x) = 1/N_y \sum_{(y=1)}^{(N_y)} \sum_{(t \in MJJAS_y)} H_s\,(x,t)$$

where $N_y = 30$ is the number of years. This metric represents the average number of Type-B-affected days per season and differs from event frequency because a multi-day event contributes one occupied day for each day on which its footprint covers the grid cell. Future changes were calculated as $\Delta D_s(x) = D_s(x) - D_{HIST}(x)$. Statistical significance of the heatwave-day changes was evaluated using a two-sided pointwise Welch's t-test applied to the daily binary Type-B occupancy samples from the future and historical periods. Diagonal hatching denotes grid cells with raw $p<0.05$, without false-discovery-rate (FDR) or other multiple-testing correction.

Persistence and intensity were derived from the tracked Type-B event catalogue. For each event i, an indicator $I_i(x)$ was defined as 1 when the event footprint occupied grid cell x on at least one day during its lifetime, and 0 otherwise. The event-characteristic composite was calculated as

$$F_{(s,X)}(x) = \left(\sum_i I_i\,(x) X_i\right) / \left(\sum_i I_i\,(x)\right)$$

where X_i represents the characteristic of event i. Persistence was represented by the total tracked event duration, whereas intensity was represented by the event-mean 2-m air-temperature anomaly. Each event was counted only once at each grid cell it intersected, irrespective of how many days it occupied that grid cell. Thus, unlike the heatwave-day metric, the persistence and intensity composites were event-equal and did not give additional weight to longer events.

Changes in persistence and intensity were calculated as $\Delta F_{(s,X)}(x) = F_{(s,X)}(x) - F_{(HIST,X)}(x)$. These feature maps were calculated only for grid cells with at least 10 distinct Type-B events in both the historical and corresponding future samples. Statistical significance was evaluated using two-sided Welch's t-tests applied to annual conditional event-feature means, with at least 10 valid annual means required in both periods.

Blocking-conditioned Type-B heatwave composites and warming-relative residuals

The coupling between Type-B heatwaves and Eurasian atmospheric blocking was assessed using the daily binary blocking mask. On each MJJAS day t, the area-weighted blocking fraction was calculated over 10°W–180°E, 40°–75°N as

$$f_B(t) = \left(\sum_x A(x)B(x,t)\right) / \left(\sum_x A(x)\right)$$

where $B(x,t)$ is the binary blocking indicator and $A(x)$ is the grid-cell area. Because blocking is an atmospheric circulation feature, both land and ocean grid cells were included in this calculation.

Type-B events were classified according to the blocking fraction on their onset date. Events with $f_B \geq 0.05$ were assigned to the strong-blocking group, corresponding to approximately $2.23 \times 10^6 km^2$ of blocked area. Events with $f_B = 0$ were assigned to the no-blocking group. Events beginning under weak blocking, $0 < f_B < 0.05$ were excluded from the primary contrast. Classification based on the onset date, rather than the occurrence of blocking at any time during the event lifetime, avoids preferentially assigning long-duration events to the blocked group simply because they have more opportunities to overlap with blocking. The 5% threshold was selected to identify substantial sector-scale blocking while retaining sufficient sample size. A sensitivity analysis using alternative blocking-area thresholds produced consistent positive blocking–Type-B heatwave associations.

For each onset group, event-equal spatial composites were calculated for persistence, intensity, mean extent, heatwave–blocking co-occurrence, and heat load. Event heat load was defined as $H_i = D_i T_i A_i$, where D_i is event duration, T_i is the event-mean 2-m air-temperature anomaly, and $A_i$is the mean event area. Event frequency was calculated separately as the number of distinct Type-B events intersecting each grid cell per MJJAS season, with years containing no events retained as zeros.

For metric X, the within-scenario blocking-conditioned contrast was defined as

$$B_{(s,X)}(x) = F^{strong}_{(s,X)}(x) - F^{none}_{(s,X)}(x)$$

where $F^{strong}_{(s,X)}$ and $F^{none}_{(s,X)}$ denote the corresponding metric for events beginning under strong-blocking and no-blocking conditions, respectively. Its future change relative to HIST was evaluated using the difference-in-differences $\Delta B_{(s,X)}(x) = B_{(s,X)}(x) - B_{(HIST,X)}(x)$. Thus, $\Delta B_{(s,X)}$ measures whether the contrast between strong-blocking-onset and no-blocking-onset heatwaves changes relative to its historical value; it is not simply the future-minus-historical change in Type-B heatwaves.

For event frequency, F was the number of distinct Type-B events intersecting each grid cell per MJJAS season, with zero-event years retained as zeros. For persistence and the other event characteristics, F was the event-equal mean among distinct events intersecting the grid cell. Grid cells were retained only when at least five distinct events were available in every required onset-group and

period combination. Statistical significance was evaluated by comparing annual strong-blocking-minus-no-blocking contrasts between the future and HIST periods using raw two-sided pointwise Welch's t-tests. At least eight valid annual contrasts were required in each period. Hatching denotes $p<0.05$, without false-discovery-rate or other multiple-testing correction.

Bootstrap uncertainty estimation for blocking–heatwave coupling metrics

Sampling uncertainty in the blocking–Type B heatwave coupling metrics was quantified using a non-parametric year-block bootstrap. Each complete May–September (MJJAS) season was treated as one resampling unit, thereby retaining the temporal dependence among days and event records within each warm season. For each simulation period, 30 MJJAS years were sampled with replacement to construct a bootstrap sample of the same length as the original period. The relevant annual numerators and denominators were then aggregated across the resampled years, and each metric was recalculated from these aggregated components rather than by resampling the previously calculated ratios. This procedure was repeated 5,000 times, and two-sided 95% confidence intervals were defined by the 2.5th and 97.5th percentiles of the resulting bootstrap distributions.

Uncertainty in future-minus-historical differences was estimated by independently resampling the historical and future periods within each bootstrap iteration and subtracting the recalculated historical metric from the corresponding future metric. A difference was considered statistically distinguishable from zero when its two-sided 95% bootstrap confidence interval excluded zero.

For the number of Type B events per blocking event, the reported point estimate was calculated by tracking contiguous blocking events over the complete 30-year period. Bootstrap resampling, however, required blocking events to be counted separately within individual years, which produced a small difference between the centre of the bootstrap distribution and the full-period estimate because events crossing annual boundaries were segmented differently. We therefore retained the full-period estimate as the reported point value and re-centred the bootstrap confidence interval on this estimate while preserving the bootstrap-derived interval offsets.

Decomposition of blocking-onset changes

To diagnose the processes underlying changes in blocking-onset occurrence, we constructed a two-dimensional precursor-state space from daily 500-hPa geopotential height (Z500). The gradient-reversal index, R_t, measures how closely the instantaneous Z500 gradients approach the two components of the Hybrid blocking criterion. For the southern and northern gradient metrics, $G_{S,t}$ and $G_{N,t}$, with blocking thresholds c_S and c_N, we defined the standardized signed margins as $M_{S,t} = \left(G_{S,t} - c_S\right)/\sigma_{S,\mathrm{HIST}}$ and $M_{N,t} = \left(c_N - G_{N,t}\right)/\sigma_{N,\mathrm{HIST}}$, respectively. The signs were oriented

so that positive values indicate satisfaction of each blocking condition. We then defined $R_t = \min(M_{S,t}, M_{N,t})$, such that positive values indicate that both gradient conditions are satisfied, whereas negative values indicate that at least one condition remains unmet. The persistent-high index H_t was defined as the standardized trailing five-day mean Z500 anomaly from $t-4$ to t. Both indices were divided into six fixed bins, with edges $-\infty, -1, -0.3, 0, 0.3, 1, \infty$, using historical scaling parameters that were subsequently applied unchanged to both warming climates. Here, r and h denote the resulting bins of R and H, respectively. Only grid-days that were unblocked at time t were included in the onset risk set, and a local onset was identified when the final Hybrid blocking mask changed from unblocked at t to blocked at $t+1$; the five-day survival requirement therefore remained embedded in the onset definition. For each joint bin (r, h), we calculated its area-weighted occupancy relative to all eligible grid-days, $\pi_s(r,h)$, and the conditional onset probability $q_s(r,h) = P(\text{onset}_{t+1} \mid R_t \in r, H_t \in h, \text{unblocked}_t)$. The regional onset rate was then reconstructed as

$$\lambda_s = \sum_{r,h} \pi_s(r,h) q_s(r,h).$$

Changes between a future climate F and historical climate H were decomposed using the exact midpoint identity,

$$\Delta\lambda = \underbrace{\sum_{r,h} \frac{q_F + q_H}{2} (\pi_F - \pi_H)}_{\text{state-occupancy contribution}} + \underbrace{\sum_{r,h} \frac{\pi_F + \pi_H}{2} (q_F - q_H)}_{\text{within-state onset-probability contribution}}$$

The analysis was performed separately for Europe (30°W–30°E), Scandinavia–Urals (30°E–90°E), Mid-East Russia (90°E–150°E) and East Siberia (150°E–180°E), and for the lower- and higher-latitude bands (LL: 45°N–60°N; HL: 60°N–75°N). Low- and high-warming responses correspond to GWL 1.5℃ and GWL 3.0℃, respectively, relative to HIST. Uncertainty in the total onset-rate change and both decomposition terms was estimated using 2,000 complete-simulation-year bootstrap replicates, with historical and future years resampled with replacement. Error bars show pointwise 95% percentile confidence intervals defined by the 2.5th and 97.5th percentiles of the bootstrap distributions; no multiple-testing correction was applied. Rates and contributions are reported as onsets per 1,000 grid-days.

North Atlantic Oscillation analysis

The North Atlantic Oscillation (NAO) analysis used a pre-calculated daily standardized NAO index. Daily 500-hPa geopotential-height anomalies over the Euro-Atlantic sector were calculated relative to a smoothed day-of-year climatology. The leading empirical orthogonal function (EOF) was

identified, and its principal-component time series was standardized to obtain the daily NAO index. The sign convention followed that of the original NAO index calculation.

The analysis was restricted to May–September (MJJAS). For each year and simulation period, the annual MJJAS mean NAO index was calculated as the mean of all daily standardized NAO values during MJJAS. NAO phases were classified using fixed standardized thresholds:

$$NAO+: NAO(t) \geq 0.5$$

$$NAO-: NAO(t) \leq -0.5$$

Days satisfying $-0.5 < NAO(t) < 0.5$ were classified as neutral. Persistent NAO events were defined as sequences of at least three consecutive days satisfying the same positive or negative phase threshold.

Changes in NAO phase days were expressed as the relative percentage change in the total number of MJJAS phase days compared with HIST: $\Delta N_s^{\pm}(\%) = 100 \times \frac{N_s^{\pm} - N_{\mathrm{HIST}}^{\pm}}{N_{\mathrm{HIST}}^{\pm}}$, where N_s^{+} and N_s^{-} denote the total numbers of NAO+ and NAO− days, respectively, in period s. Thus, the displayed values represent relative changes in phase-day counts rather than percentage-point changes in their seasonal fractions. For statistical inference, annual MJJAS mean NAO indices and annual fractions of NAO+ and NAO− days were used as the statistical samples. Each future period was compared with HIST using a two-sided Welch's t-test.

Background meridional potential-vorticity gradient under non-blocking conditions

To characterize changes in the large-scale low-frequency dynamical background, the meridional potential-vorticity gradient at 200 hPa (PV_y) was calculated following the nonlinear multiscale interaction framework for atmospheric blocking (D. Luo et al., 2025; D. Luo and Zhang, 2020). Physically, PV_y characterizes the background dynamical environment for the propagation and dispersion of large-scale atmospheric disturbances. A smaller PV_y generally corresponds to weaker energy dispersion and stronger localization of circulation anomalies, favouring their persistence and the associated weather extremes. Daily zonal winds at 200, 500 and 850 hPa were first filtered using a 60-day low-pass filter to remove higher-frequency circulation variability and isolate the slowly varying background flow. Annual MJJAS mean filtered zonal winds ($\overline{U}_{200}$, $\overline{U}_{500}$ and $\overline{U}_{850}$) were then calculated for each year and used in the PV_y diagnosis.

$$\mathrm{PV}y = \beta - \frac{\partial^2 \overline{U}_{200}}{\partial y^2} - \frac{f_0^2}{N_{200}^2}\frac{\partial^2 \overline{U}}{\partial z^2}$$

where $\beta = \frac{2\Omega\cos\phi}{a}$ and $f_0 = 2\Omega\sin(60°)$. Here, Ω is Earth's angular velocity, a is Earth's radius, φ is latitude, and N_{200}^2 is the squared Brunt–Väisälä frequency at 200 hPa. The meridional and vertical wind-curvature terms represent contributions from the horizontal and vertical structures of the background zonal flow to the meridional potential-vorticity gradient, respectively (D. Luo et al., 2019; D. Luo and Zhang, 2020)

The static stability at 200 hPa was derived from the scenario-specific MJJAS climatological temperature field as

$$N_{200}^2 = -\frac{g^2}{R_d T\theta}\frac{\partial\theta}{\partial \ln p}$$

where g is gravitational acceleration, R_d is the gas constant for dry air, T is air temperature, θ is potential temperature, and p is pressure. The vertical wind-curvature term was estimated from the annual mean zonal winds at 200, 500 and 850 hPa using a quadratic approximation in geopotential height.

Because latitude was stored in degrees, the second meridional derivative of the 200-hPa zonal wind was converted to physical-distance coordinates as

$$\frac{\partial^2\overline{U}_{200}}{\partial y^2} = \left(\frac{180}{\pi a}\right)^2 \frac{\partial^2\overline{U}_{200}}{\partial\phi_{\mathrm{deg}}^2}$$

Scenario climatologies were obtained by averaging the annual PV_y fields. Statistical significance was assessed at each grid cell using a two-sided Welch's t-test applied to the annual PV_y samples from GWL 3.0 °C and GWL 1.5 °C. Hatching denotes grid cells with raw $p<0.05$, without false-discovery-rate or other multiple-testing correction. All fields were displayed on the native model grid without spatial smoothing or interpolation. The 88–90°N latitude rows were excluded because the pole-adjacent second-order meridional derivative is particularly sensitive to the finite-difference boundary treatment. For visualization,PV_y was expressed in units of $10^{-11}s^{-1}m^{-1}$.

References

Abnett, K., 2026, June 23: Explainer: What is the "Omega Block" causing Europe's intense heatwave? *Reuters*. https://www.reuters.com/business/environment/what-is-omega-block-causing-europes-intense-heatwave-2026-06-23/

Athanasiadis, P. J. et al., 2020: Decadal predictability of North Atlantic blocking and the NAO. *Npj Climate and Atmospheric Science*, **3(1)**, 20. doi: 10.1038/s41612-020-0120-6

Barriopedro, D., R. García-Herrera, C. Ordóñez, D. G. Miralles and S. Salcedo-Sanz, 2023: Heat Waves: Physical Understanding and Scientific Challenges. *Reviews of Geophysics*, **61(2)**, e2022RG000780. doi: 10.1029/2022RG000780

Bevacqua, E., E. Fischer, J. Sillmann and J. Zscheischler, 2026: Moderate global warming does not rule out extreme global climate outcomes. *Nature*, **651(8107)**, 946–953. doi: 10.1038/s41586-026-10237-9

Castruccio, F. S. et al., 2024a: *MESACLIP: A 10-member ensemble of CESM HR historical (1920-2005) simulations* [Dataset]. NSF National Center for Atmospheric Research. doi: 10.5065/7N1X-K278

Castruccio, F. S. et al., 2024b: *MESACLIP: A 10-member ensemble of CESM HR RCP 8.5 (2006-2100) simulations* [Dataset]. NSF National Center for Atmospheric Research. doi: 10.5065/PNCR-5S34

Castruccio, F. S. et al., 2025: *iPOGS: CESM HR simulations under the RCP 2.6 and RCP 4.5 (2006-2100) scenario* [Dataset]. NSF National Center for Atmospheric Research. doi: 10.5065/PNFP-T325

Chang, P. et al., 2020: An Unprecedented Set of High-Resolution Earth System Simulations for Understanding Multiscale Interactions in Climate Variability and Change. *Journal of Advances in Modeling Earth Systems*, **12(12)**, e2020MS002298. doi: 10.1029/2020MS002298

Chang, P. et al., 2026: Future extreme precipitation amplified by intensified mesoscale moisture convergence. *Nature Geoscience*, **19(1)**, 33–41. doi: 10.1038/s41561-025-01859-1

Copernicus Climate Change Service, 2026, July 9: *Copernicus: Record heatwave brings hottest June for western Europe during second-warmest June globally* [Press release]. Copernicus Climate Change Service. https://climate.copernicus.eu/copernicus-record-heatwave-brings-hottest-june-western-europe-during-second-warmest-june-globally

Coumou, D., G. Di Capua, S. Vavrus, L. Wang and S. Wang, 2018: The influence of Arctic amplification on mid-latitude summer circulation. *Nature Communications*, **9(1)**, 2959. doi: 10.1038/s41467-018-05256-8

Davini, P. and F. D'Andrea, 2016: Northern Hemisphere Atmospheric Blocking Representation in Global Climate Models: Twenty Years of Improvements? *Journal of Climate*, **29(24)**, 8823–8840. doi: 10.1175/JCLI-D-16-0242.1

Davini, P. and F. D'Andrea, 2020: From CMIP3 to CMIP6: Northern Hemisphere Atmospheric Blocking Simulation in Present and Future Climate. *Journal of Climate*, **33(23)**, 10021–10038. doi: 10.1175/JCLI-D-19-0862.1

Deser, C., 2020: "Certain Uncertainty: The Role of Internal Climate Variability in Projections of Regional Climate Change and Risk Management." *Earth's Future*, **8(12)**, e2020EF001854. doi: 10.1029/2020EF001854

Domeisen, D. I. et al., 2023: Prediction and projection of heatwaves. *Nature Reviews Earth & Environment*, **4(1)**, 36–50.

Dong, B., R. T. Sutton, L. Shaffrey and B. Harvey, 2022: Recent decadal weakening of the summer Eurasian westerly jet attributable to anthropogenic aerosol emissions. *Nature Communications*, **13(1)**, 1148. doi: 10.1038/s41467-022-28816-5

Fang, B. and M. Lu, 2024: Escalated Risk of Concurrent Eurasian Heatwaves Under Recurrent Rossby Wave Patterns. *Journal of Geophysical Research: Atmospheres*, **129(24)**, e2024JD042437. doi: 10.1029/2024JD042437

Forzieri, G. et al., 2018: Escalating impacts of climate extremes on critical infrastructures in Europe. *Global Environmental Change*, **48**, 97–107. doi: 10.1016/j.gloenvcha.2017.11.007

Gao, Y. et al., 2023: More Frequent and Persistent Heatwaves Due To Increased Temperature Skewness Projected by a High-Resolution Earth System Model. *Geophysical Research Letters*, **50(18)**, e2023GL105840. doi: 10.1029/2023GL105840

Gao, Y. et al., 2025: Enhanced Simulation of Atmospheric Blocking in a High-Resolution Earth System Model: Projected Changes and Implications for Extreme Weather Events. *Journal of Geophysical Research: Atmospheres*, **130(3)**, e2024JD042045. doi: 10.1029/2024JD042045

Good, P. et al., 2015: Nonlinear regional warming with increasing CO2 concentrations. *Nature Climate Change*, **5(2)**, 138–142. doi: 10.1038/nclimate2498

Groisman, P. et al., 2018: Dryland belt of Northern Eurasia: contemporary environmental changes and their consequences. *Environmental Research Letters*, **13(11)**, 115008. doi: 10.1088/1748-9326/aae43c

Gu, X. et al., 2019: Intensification and Expansion of Soil Moisture Drying in Warm Season Over Eurasia Under Global Warming. *Journal of Geophysical Research: Atmospheres*, **124(7)**, 3765–3782. doi: 10.1029/2018JD029776

Hawkins, E. and R. Sutton, 2009: The Potential to Narrow Uncertainty in Regional Climate Predictions. *Bulletin of the American Meteorological Society*, **90(8)**, 1095–1108. doi: 10.1175/2009BAMS2607.1

Hersbach, H. et al., 2020: The ERA5 global reanalysis. *Quarterly Journal of the Royal Meteorological Society*, **146(730)**, 1999–2049. doi: 10.1002/qj.3803

IPCC, 2021: *Climate Change 2021: The Physical Science Basis. Contribution of Working Group I to the Sixth Assessment Report of the Intergovernmental Panel on Climate Change* (V. Masson-Delmotte et al., Eds.). Cambridge University Press. doi: 10.1017/9781009157896

Jain, S. et al., 2023: Importance of internal variability for climate model assessment. *Npj Climate and Atmospheric Science*, **6(1)**, 68. doi: 10.1038/s41612-023-00389-0

Kautz, L.-A. et al., 2022: Atmospheric blocking and weather extremes over the Euro-Atlantic sector – a review. *Weather and Climate Dynamics*, **3(1)**, 305–336. doi: 10.5194/wcd-3-305-2022

Kornhuber, K. et al., 2020: Amplified Rossby waves enhance risk of concurrent heatwaves in major breadbasket regions. *Nature Climate Change*, **10(1)**, 48–53. doi: 10.1038/s41558-019-0637-z

Lehner, F. and S. Coats, 2021: Does Regional Hydroclimate Change Scale Linearly With Global Warming? *Geophysical*

Research Letters, **48(23)**, e2021GL095127. doi: 10.1029/2021GL095127

Liang, Y.-C., L. M. Polvani and I. Mitevski, 2022: Arctic amplification, and its seasonal migration, over a wide range of abrupt CO2 forcing. *Npj Climate and Atmospheric Science*, **5(1)**, 14. doi: 10.1038/s41612-022-00228-8

Liu, C., V. M. Galfi, F. Cai, W. A. Robinson and D. Coumou, 2025: The role of Rossby wave dynamics in spatially compounding heatwaves in mid-summer 2023. *Environmental Research Letters*, **20(3)**, 034052. doi: 10.1088/1748-9326/adb768

Liu, P. et al., 2018: Climatology of tracked persistent maxima of 500-hPa geopotential height. *Climate Dynamics*, **51(1–2)**, 701–717. doi: 10.1007/s00382-017-3950-0

Liu, P., 2020: Climatologies of blocking highs detected by a unified Eddy-ABS approach. *Climate Dynamics*, **54(1)**, 1197–1215. doi: 10.1007/s00382-019-05053-z

Lo, S.-H., C.-T. Chen, S. Russo, W.-R. Huang and M.-F. Shih, 2021: Tracking heatwave extremes from an event perspective. *Weather and Climate Extremes*, **34**, 100371. doi: 10.1016/j.wace.2021.100371

Lohmann, R., C. Purr and B. Ahrens, 2024: Northern Hemisphere Atmospheric Blocking in CMIP6 Climate Projections Using a Hybrid Index. *Journal of Climate*, **37(24)**, 6605–6625. doi: 10.1175/JCLI-D-23-0589.1

Luo, D., B. Luo and W. Zhang, 2023: A Perspective on the Evolution of Atmospheric Blocking Theories: From Eddy-Mean flow Interaction to Nonlinear Multiscale Interaction. *Advances in Atmospheric Sciences*, **40(4)**, 553–569. doi: 10.1007/s00376-022-2194-z

Luo, D., Y. Yao and A. Dai, 2015: *Decadal Relationship between European Blocking and the North Atlantic Oscillation during 1978–2011. Part I: Atlantic Conditions*. doi: 10.1175/JAS-D-14-0039.1

Luo, D., Y. Yao, A. Dai and S. B. Feldstein, 2015: *The Positive North Atlantic Oscillation with Downstream Blocking and Middle East Snowstorms: The Large-Scale Environment*. doi: 10.1175/JCLI-D-15-0184.1

Luo, D. and W. Zhang, 2020: A Nonlinear Multiscale Theory of Atmospheric Blocking: Dynamical and Thermodynamic Effects of Meridional Potential Vorticity Gradient. *Journal of the Atmospheric Sciences*, **77(7)**, 2471–2500. doi: 10.1175/JAS-D-20-0004.1

Luo, D., W. Zhang and B. Luo, 2025: A Nonlinear Multi-Scale Interaction Model for Atmospheric Blocking: A Tool for Exploring the Impact of Changing Climate on Mid-to-High Latitude Weather Extremes. *Advances in Atmospheric Sciences*, **42(10)**, 2018–2035. doi: 10.1007/s00376-024-4435-9

Luo, D., W. Zhang, L. Zhong and A. Dai, 2019: A Nonlinear Theory of Atmospheric Blocking: A Potential Vorticity Gradient View. *Journal of the Atmospheric Sciences*, **76(8)**, 2399–2427. doi: 10.1175/JAS-D-18-0324.1

Luo, M. et al., 2022: Two different propagation patterns of spatiotemporally contiguous heatwaves in China. *Npj Climate and Atmospheric Science*, **5(1)**, 89. doi: 10.1038/s41612-022-00313-y

Luo, M. et al., 2024: Anthropogenic forcing has increased the risk of longer-traveling and slower-moving large contiguous heatwaves. *Science Advances*, **10(13)**, eadl1598. doi: 10.1126/sciadv.adl1598

Ma, K. et al., 2024: Anthropogenic forcing intensified internally driven concurrent heatwaves in August 2022 across the

Northern Hemisphere. *Npj Climate and Atmospheric Science*, **7(1)**, 290. doi: 10.1038/s41612-024-00828-6

Maher, N., F. Lehner and J. Marotzke, 2020: Quantifying the role of internal variability in the temperature we expect to observe in the coming decades. *Environmental Research Letters*, **15(5)**, 054014. doi: 10.1088/1748-9326/ab7d02

Masato, G., B. J. Hoskins and T. Woollings, 2013: Winter and Summer Northern Hemisphere Blocking in CMIP5 Models. *Journal of Climate*, **26(18)**, 7044–7059. doi: 10.1175/JCLI-D-12-00466.1

Maule, C. F., T. Mendlik and O. B. Christensen, 2017: The effect of the pathway to a two degrees warmer world on the regional temperature change of Europe. *Climate Services*, **7**, 3–11. doi: 10.1016/j.cliser.2016.07.002

Ono, J., M. Watanabe, Y. Komuro, H. Tatebe and M. Abe, 2022: Enhanced Arctic warming amplification revealed in a low-emission scenario. *Communications Earth & Environment*, **3(1)**, 27. doi: 10.1038/s43247-022-00354-4

Pfahl, S. and H. Wernli, 2012: Quantifying the relevance of atmospheric blocking for co-located temperature extremes in the Northern Hemisphere on (sub-)daily time scales. *Geophysical Research Letters*, **39(12)**. doi: 10.1029/2012GL052261

Riahi, K. et al., 2011: RCP 8.5—A scenario of comparatively high greenhouse gas emissions. *Climatic Change*, **109(1)**, 33. doi: 10.1007/s10584-011-0149-y

Rogers, C. D. W., K. Kornhuber, S. E. Perkins-Kirkpatrick, P. C. Loikith and D. Singh, 2022: Sixfold Increase in Historical Northern Hemisphere Concurrent Large Heatwaves Driven by Warming and Changing Atmospheric Circulations. *Journal of Climate*, **35(3)**, 1063–1078. doi: 10.1175/JCLI-D-21-0200.1

Rousi, E., K. Kornhuber, G. Beobide-Arsuaga, F. Luo and D. Coumou, 2022: Accelerated western European heatwave trends linked to more-persistent double jets over Eurasia. *Nature Communications*, **13(1)**, 3851. doi: 10.1038/s41467-022-31432-y

Ruffault, J. et al., 2020: Increased likelihood of heat-induced large wildfires in the Mediterranean Basin. *Scientific Reports*, **10(1)**, 13790. doi: 10.1038/s41598-020-70069-z

Schiemann, R. et al., 2020: Northern Hemisphere blocking simulation in current climate models: evaluating progress from the Climate Model Intercomparison Project Phase 5 to 6 and sensitivity to resolution. *Weather and Climate Dynamics*, **1(1)**, 277–292. doi: 10.5194/wcd-1-277-2020

Shepherd, T. G., 2014: Atmospheric circulation as a source of uncertainty in climate change projections. *Nature Geoscience*, **7(10)**, 703–708. doi: 10.1038/ngeo2253

Shepherd, T. G. et al., 2018: Storylines: an alternative approach to representing uncertainty in physical aspects of climate change. *Climatic Change*, **151(3)**, 555–571. doi: 10.1007/s10584-018-2317-9

Taylor, K. E., R. J. Stouffer and G. A. Meehl, 2012: An Overview of CMIP5 and the Experiment Design. *Bulletin of the American Meteorological Society*, **93(4)**, 485–498. doi: 10.1175/BAMS-D-11-00094.1

Undorf, S., M. A. Bollasina and G. C. Hegerl, 2018: Impacts of the 1900–74 Increase in Anthropogenic Aerosol Emissions from North America and Europe on Eurasian Summer Climate. *Journal of Climate*, **31(20)**, 8381–8399. doi: 10.1175/JCLI-D-17-0850.1

Van Vuuren, D. P. et al., 2011: RCP2.6: exploring the possibility to keep global mean temperature increase below 2°C. *Climatic Change*, **109(1–2)**, 95–116. doi: 10.1007/s10584-011-0152-3

Vicedo-Cabrera, A. M. et al., 2021: The burden of heat-related mortality attributable to recent human-induced climate change. *Nature Climate Change*, **11(6)**, 492–500. doi: 10.1038/s41558-021-01058-x

Wang, L. et al., 2026: Gaps and ways forward in atmospheric blocking and extreme weather research. *Nature Communications*, **17(1)**, 2873. doi: 10.1038/s41467-026-70487-z

Wang, M. et al., 2025: Evidence for preferred propagating terrestrial heatwave pathways due to Rossby wave activity. *Nature Communications*, **16(1)**, 4742. doi: 10.1038/s41467-025-60104-w

Woollings, T. et al., 2018: Blocking and its Response to Climate Change. *Current Climate Change Reports*, **4(3)**, 287–300. doi: 10.1007/s40641-018-0108-z

Zappa, G. and T. G. Shepherd, 2017: Storylines of Atmospheric Circulation Change for European Regional Climate Impact Assessment. *Journal of Climate*, **30(16)**, 6561–6577. doi: 10.1175/JCLI-D-16-0807.1

Zhang, S. et al., 2020: Optimizing high-resolution Community Earth System Model on a heterogeneous many-core supercomputing platform. *Geoscientific Model Development*, **13(10)**, 4809–4829. doi: 10.5194/gmd-13-4809-2020

Zhong, J. et al., 2025: Plausible global emissions scenario for 2 °C aligned with China's net-zero pathway. *Nature Communications*, **16(1)**, 8102. doi: 10.1038/s41467-025-62983-5

Zhu, S. et al., 2026: Decadal doubling of Siberian methane emissions due to warming-induced fires and methanogenesis. *Science*, **393(6811)**, 615–621. doi: 10.1126/science.aea5828

Extended Data

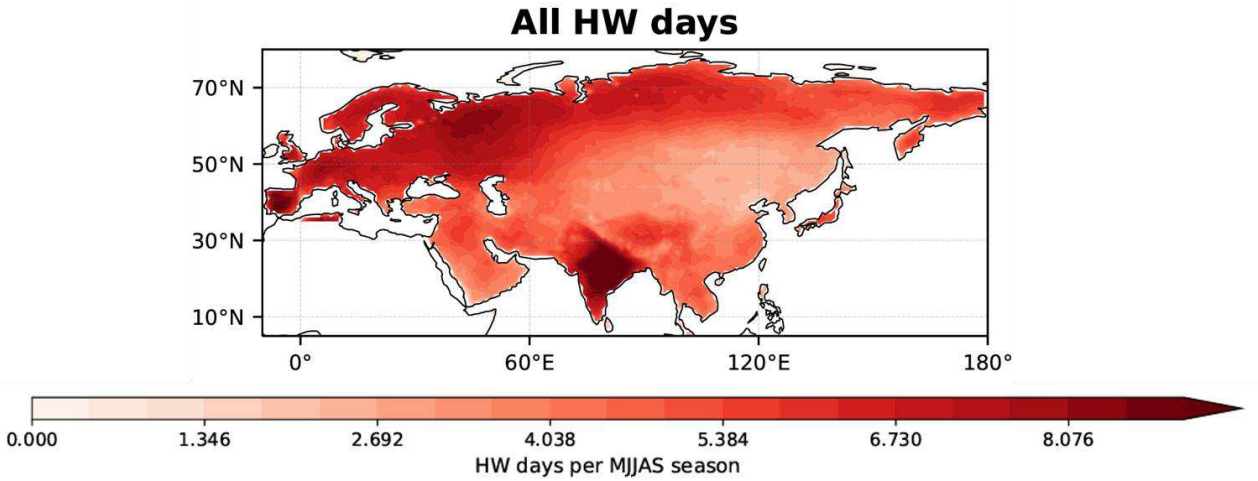

Extended Data Fig.1. Spatial distribution of total Eurasian heatwave occurrence. Spatial distribution of the mean annual number of heatwave days during May–September (MJJAS) over Eurasia for 1975–2025. Values indicate the number of heatwave days per MJJAS season at each grid cell, including heatwave days associated with both Type A and Type B events.

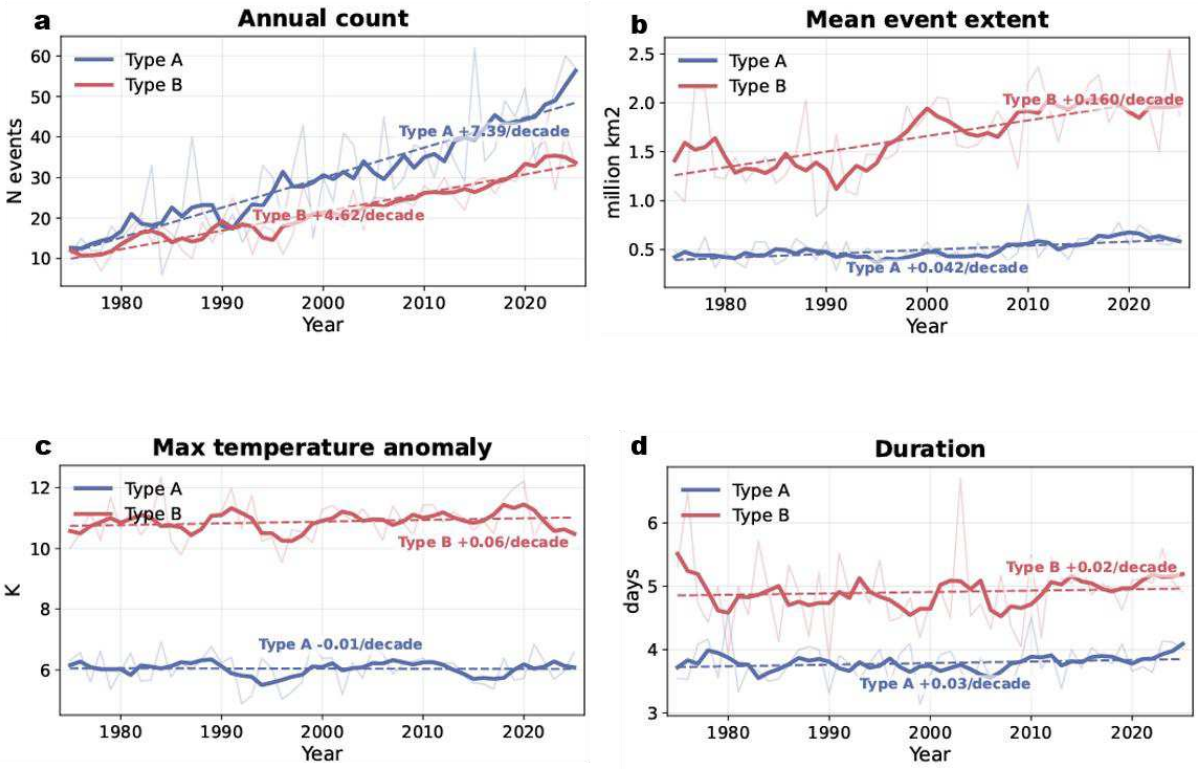

Extended Data Fig.2. Historical trends in additional characteristics of Type A and Type B Eurasian heatwaves. a–d, Historical changes in event-scale properties of Type A and Type B heatwaves during 1975–2025: **a**, annual event count; **b**, mean event spatial extent; **c**, maximum

temperature anomaly; and **d,** event duration. Thin lines show annual values, thick lines indicate 5-year centred rolling means, and dashed lines denote ordinary least-squares (OLS) linear trends. Trend magnitudes are labelled for each event type.

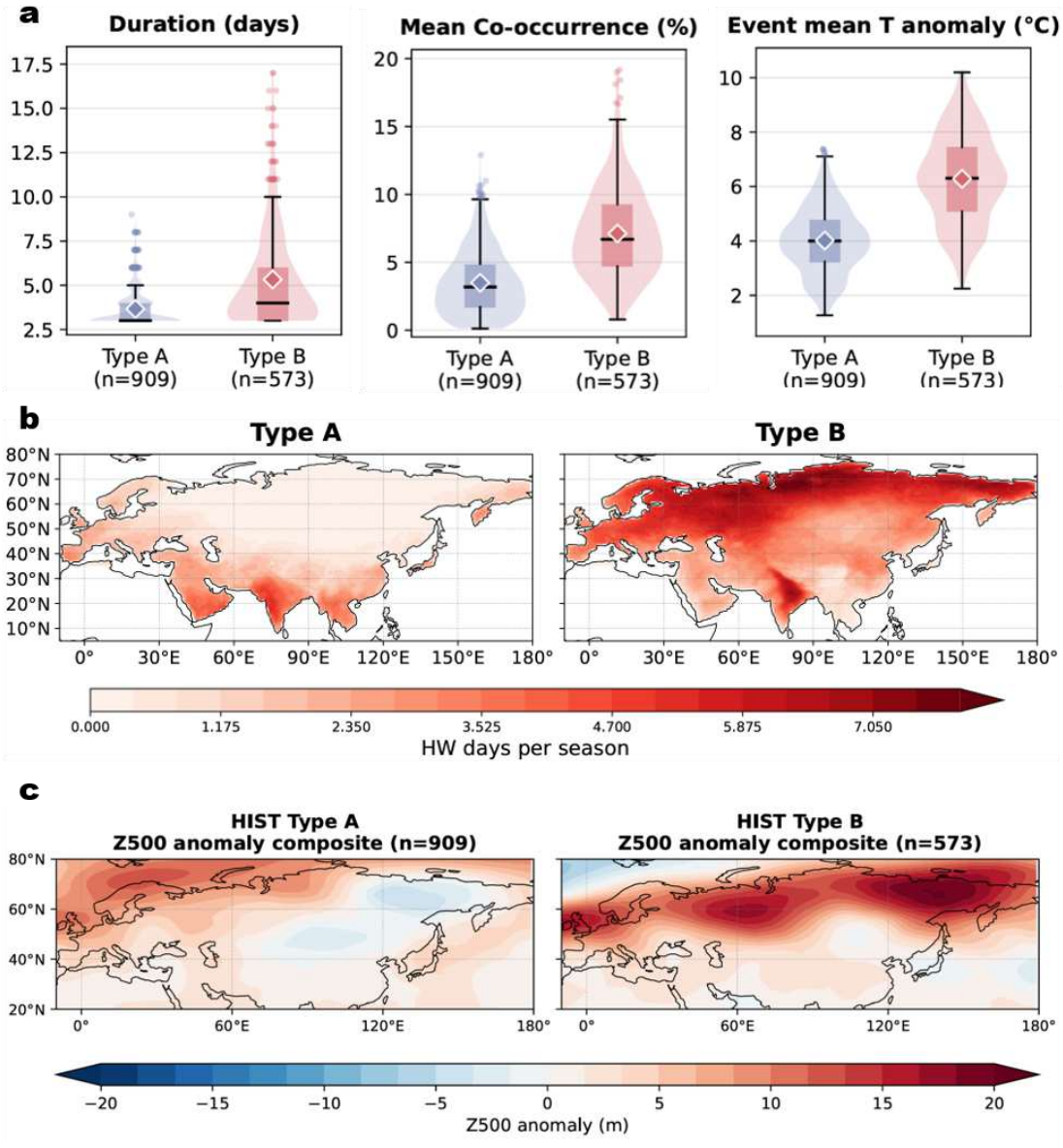

Extended Data Fig. 3. Historical representation of the two Eurasian heatwave types in CESM-HR. a, Distributions of event duration, mean spatial co-occurrence and event-mean temperature anomaly for Type A and Type B heatwaves identified in the CESM-HR historical simulation (1975–2004). Violin plots show the distributions; boxes indicate the interquartile range, horizontal lines the median, whiskers extend to 1.5 times the interquartile range, diamonds denote the mean, and points represent individual events. Sample sizes indicate the total number of events identified during the 30-year period. **b**, Spatial distributions of the mean annual number of May–September (MJJAS) heatwave

days associated with Type A and Type B events. **c**, Event-composite 500-hPa geopotential height (Z500) anomalies associated with Type A and Type B heatwaves, calculated relative to the 1975–2004 MJJAS climatology. Together, these event-scale distributions and spatial composites show that CESM-HR captures the principal differences between the two heatwave types and their associated large-scale circulation patterns identified in ERA5.

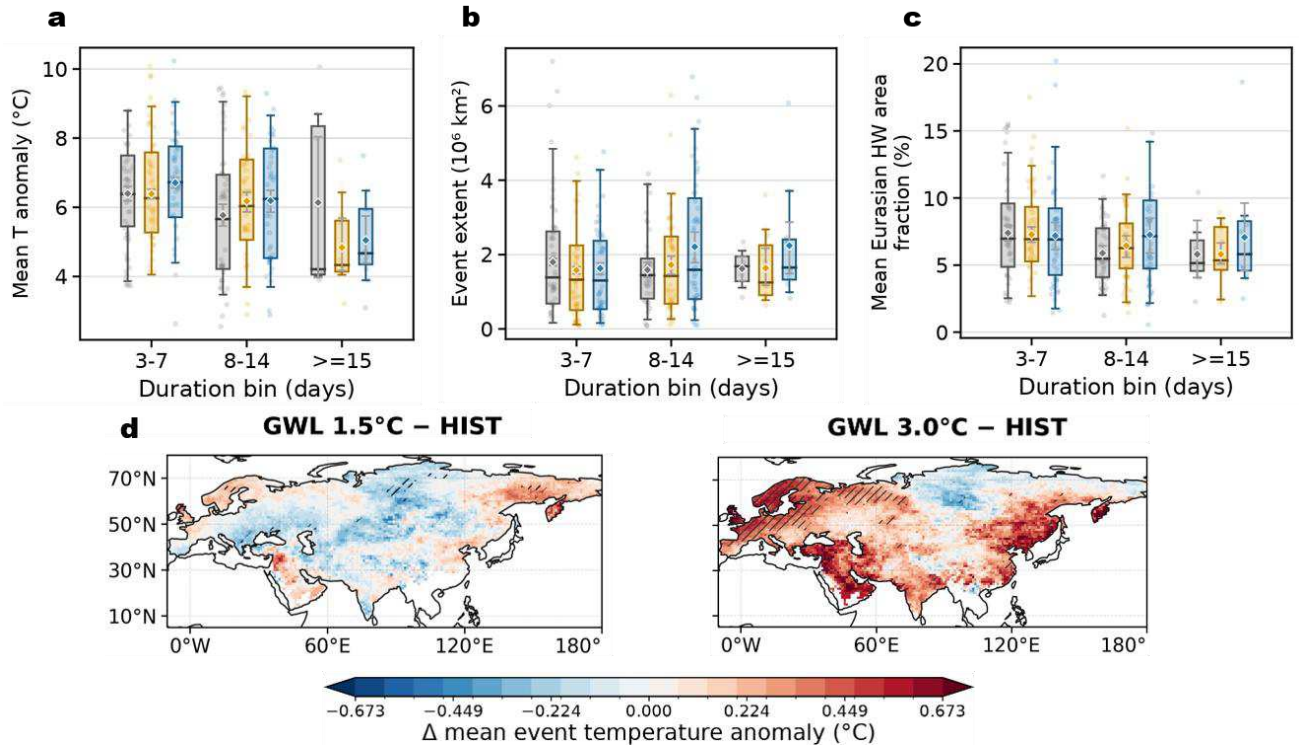

Extended Data Fig. 4. Duration-dependent intensity and spatial characteristics of organized Eurasian heatwaves. Characteristics of organized heatwaves simulated by the high-resolution Community Earth System Model (CESM-HR) for the historical period (HIST; 1975–2004) and two mid-century warming states corresponding to approximately 1.5 °C and 3.0 °C of global warming above the pre-industrial baseline, represented by 2041–2070 under RCP2.6 and RCP8.5, respectively. Events are grouped into three duration classes: 3–7, 8–14 and ≥15 days. **a–c**, Distributions of **a**, event-mean temperature anomaly, **b**, event spatial extent and **c**, mean Eurasian heatwave area fraction for HIST (grey), GWL 1.5 °C (yellow) and GWL 3.0 °C (blue). Boxes indicate the interquartile range, horizontal lines the median, whiskers extend to 1.5 times the interquartile range, and points represent individual events. Diamonds denote the mean, with coloured error bars showing two-sided 95% confidence intervals estimated from 2,000 bootstrap resamples of complete MJJAS years within each 30-year period. **d,e**, Future-minus-historical changes in mean event temperature anomaly for **d**, GWL 1.5 °C and **e**, GWL 3.0 °C. Hatching indicates grid cells where future and historical values differ at the 95% confidence level based on two-sided Welch's *t*-tests ($p < 0.05$).

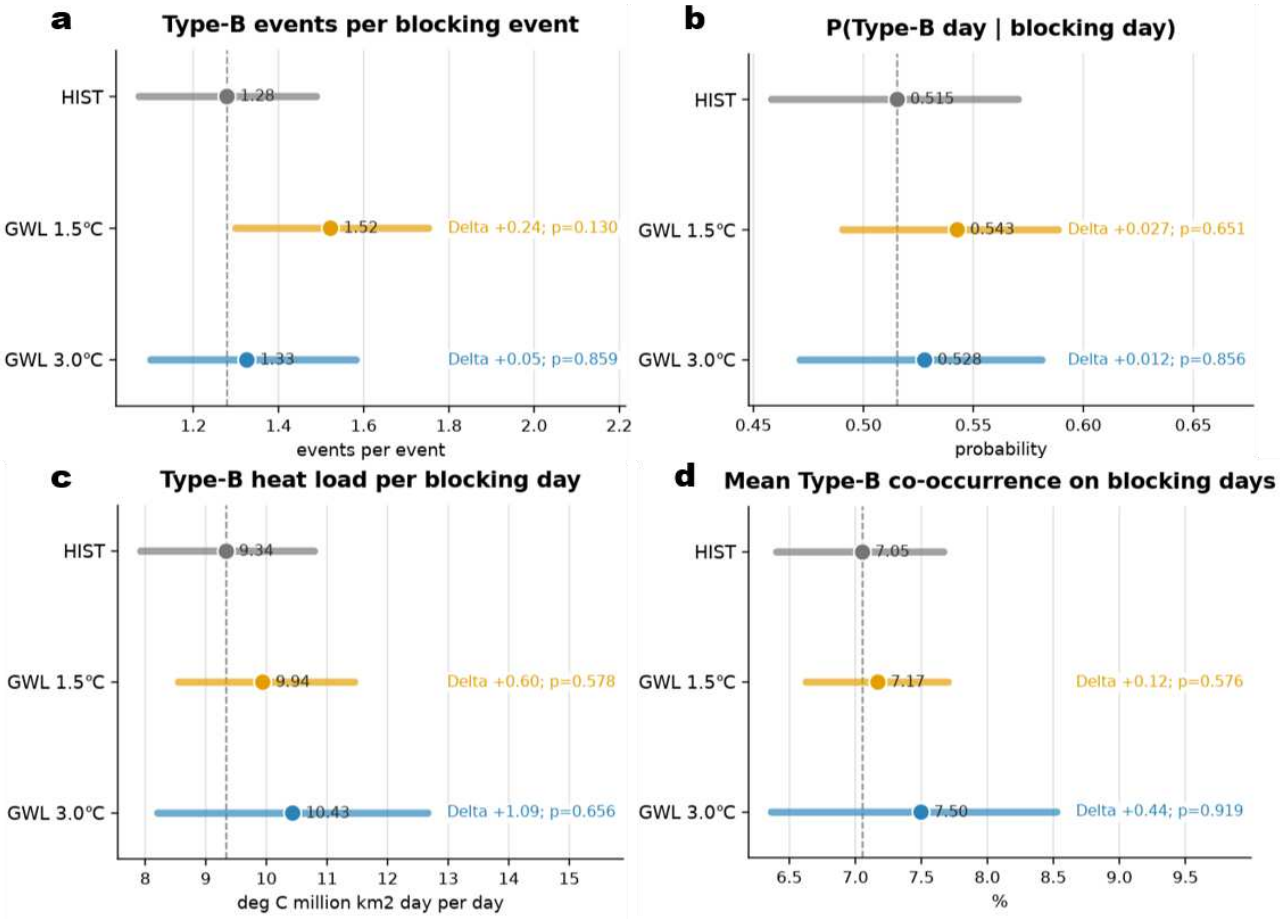

Extended Data Fig. 5. Changes in blocking–organized heatwave coupling across two mid-century warming states. Blocking–organized heatwave relationships simulated by the high-resolution Community Earth System Model (CESM-HR) are compared between the historical period (HIST; 1975–2004) and two mid-century warming states corresponding to approximately 1.5°C and 3.0°C of global warming above the pre-industrial baseline, represented by 2041–2070 under RCP2.6 and RCP8.5, respectively. Shown are **a**, the number of organized heatwave events per blocking event; **b**, the conditional probability of an organized heatwave day given a blocking day, P(organized heatwave day | blocking day); **c**, organized heatwave heat load per blocking day; and **d**, mean organized heatwave spatial co-occurrence on blocking days. Points show estimates calculated over the full 30-year periods, horizontal lines denote two-sided 95% confidence intervals estimated using year-block bootstrap resampling, and vertical dashed lines indicate HIST estimates. Annotations report future-minus-HIST differences and unadjusted p values from two-sided Welch's t-tests; no significance symbols are shown. Organized heatwave heat load is calculated as the area-weighted sum of temperature anomalies over all affected grid cells and event days and is expressed in °C million km^2 day per blocking day. Spatial co-occurrence is defined as the fraction of the Eurasian domain simultaneously affected by organized heatwaves on blocking days.

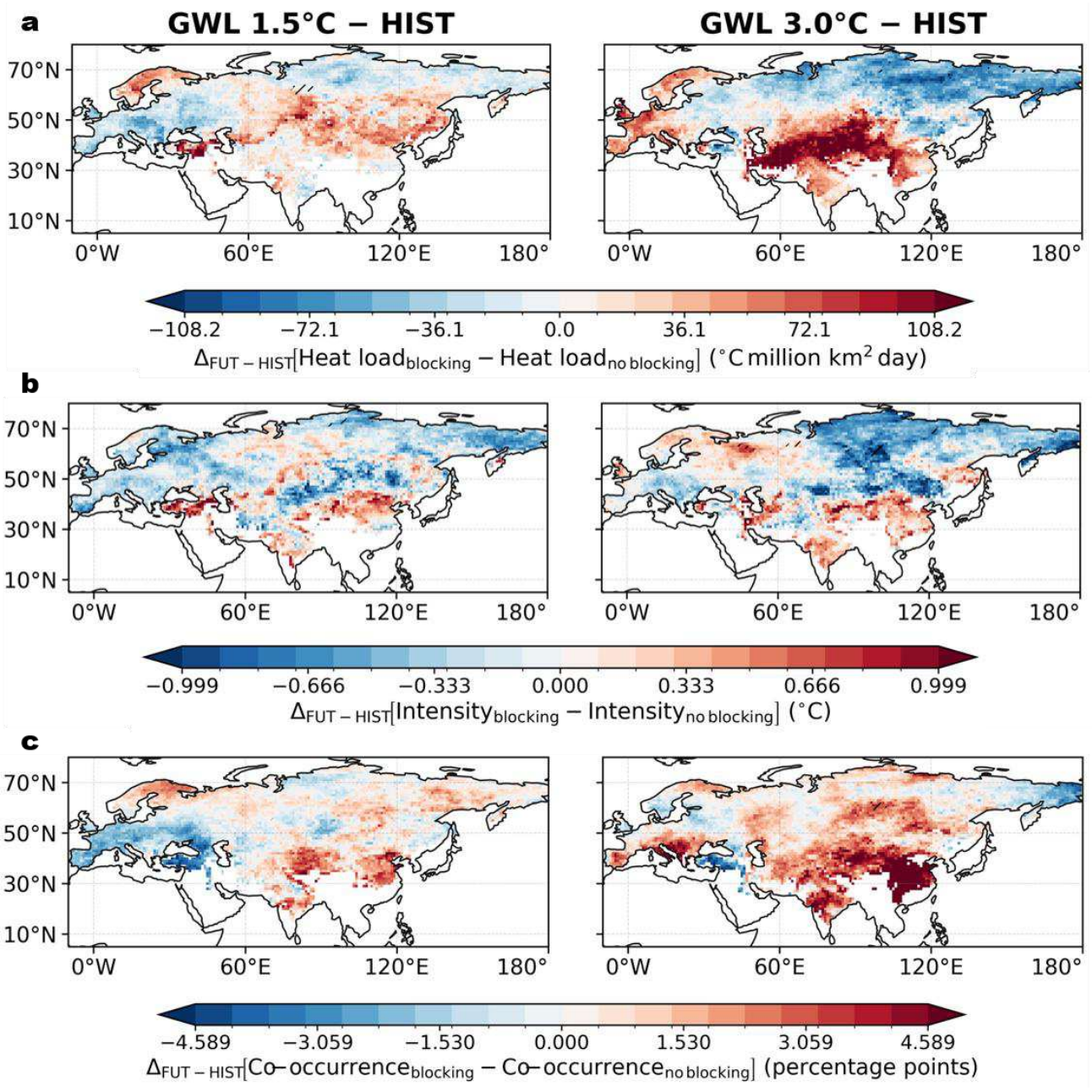

Extended Data Fig. 6. Changes in blocking-associated contrasts in organized heatwave characteristics across two mid-century warming states. Spatial changes in the relationship between blocking and organized Eurasian heatwave characteristics simulated by the high-resolution Community Earth System Model (CESM-HR), comparing two mid-century warming states with the historical period (HIST; 1975–2004). The warming states correspond to approximately 1.5°C and 3.0°C of global warming above the pre-industrial baseline and are represented by 2041–2070 under RCP2.6 and RCP8.5, respectively. Each row shows future-minus-HIST changes for GWL 1.5°C (left) and GWL 3.0°C (right). From top to bottom, panels show changes in the strong-blocking versus no-blocking contrast in **a**, organized heatwave heat load, **b**, organized heatwave intensity and **c**, organized

heatwave spatial co-occurrence. For each characteristic X, the plotted quantity is $[X_{\text{strong blocking}} - X_{\text{no blocking}}]_\text{future} - [X_{\text{strong blocking}} - X_{\text{no blocking}}]_HIST$. Heat load is calculated as the area-weighted sum of temperature anomalies over all affected grid cells and event days. Intensity is defined as the mean temperature anomaly of organized heatwaves, and spatial co-occurrence as the fraction of the Eurasian domain simultaneously affected by organized heatwaves. Hatching indicates grid cells where future and historical contrast values differ at the 95% confidence level according to two-sided Welch's t-tests ($p < 0.05$).

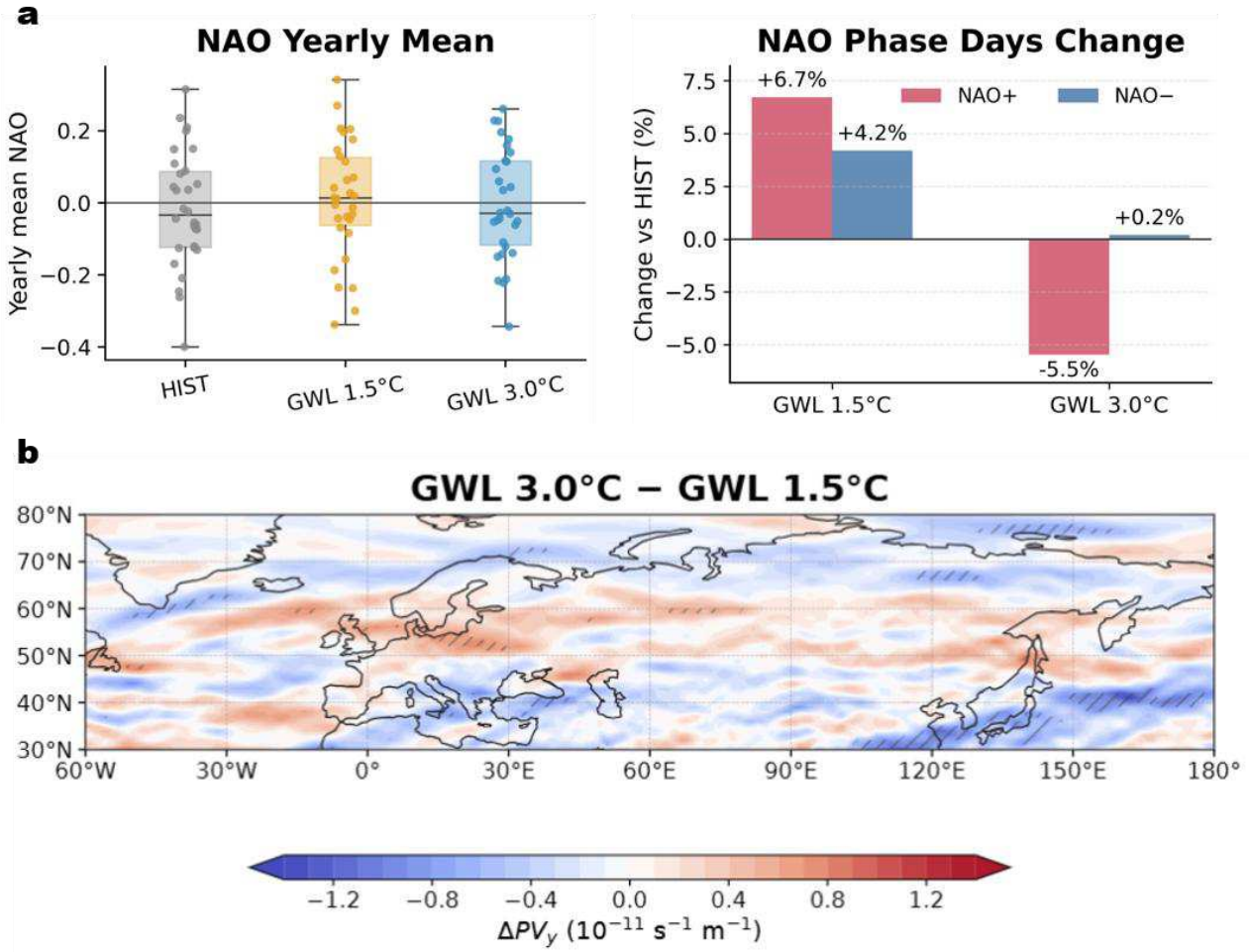

Extended Data Fig. 7. Changes in the North Atlantic Oscillation and meridional potential-vorticity gradient across two mid-century warming states. Large-scale circulation changes simulated by the high-resolution Community Earth System Model (CESM-HR) are compared between the historical period (HIST; 1975–2004) and two mid-century warming states corresponding to approximately 1.5°C and 3.0°C of global warming above the pre-industrial baseline, represented by 2041–2070 under RCP2.6 and RCP8.5, respectively. **a**, Changes in the North Atlantic Oscillation

(NAO). The upper panel shows distributions of annual-mean NAO indices for HIST (grey), GWL 1.5°C (yellow) and GWL 3.0°C (blue). Points represent individual years, boxes indicate the interquartile range, horizontal lines the median, whiskers extend to 1.5 times the interquartile range, and diamonds denote the mean. The lower panel shows future-minus-HIST changes in the occurrence frequency of positive (NAO+) and negative (NAO-) phases. **b**, Difference in the meridional potential-vorticity gradient between GWL 3.0°C and GWL 1.5°C. Hatching indicates regions where the difference is statistically significant at the 95% confidence level according to two-sided Welch's t-tests ($p<0.05$). The meridional potential-vorticity gradient is calculated following the definition of Luo et al. and characterizes the background dynamical environment influencing the development and persistence of atmospheric blocking.

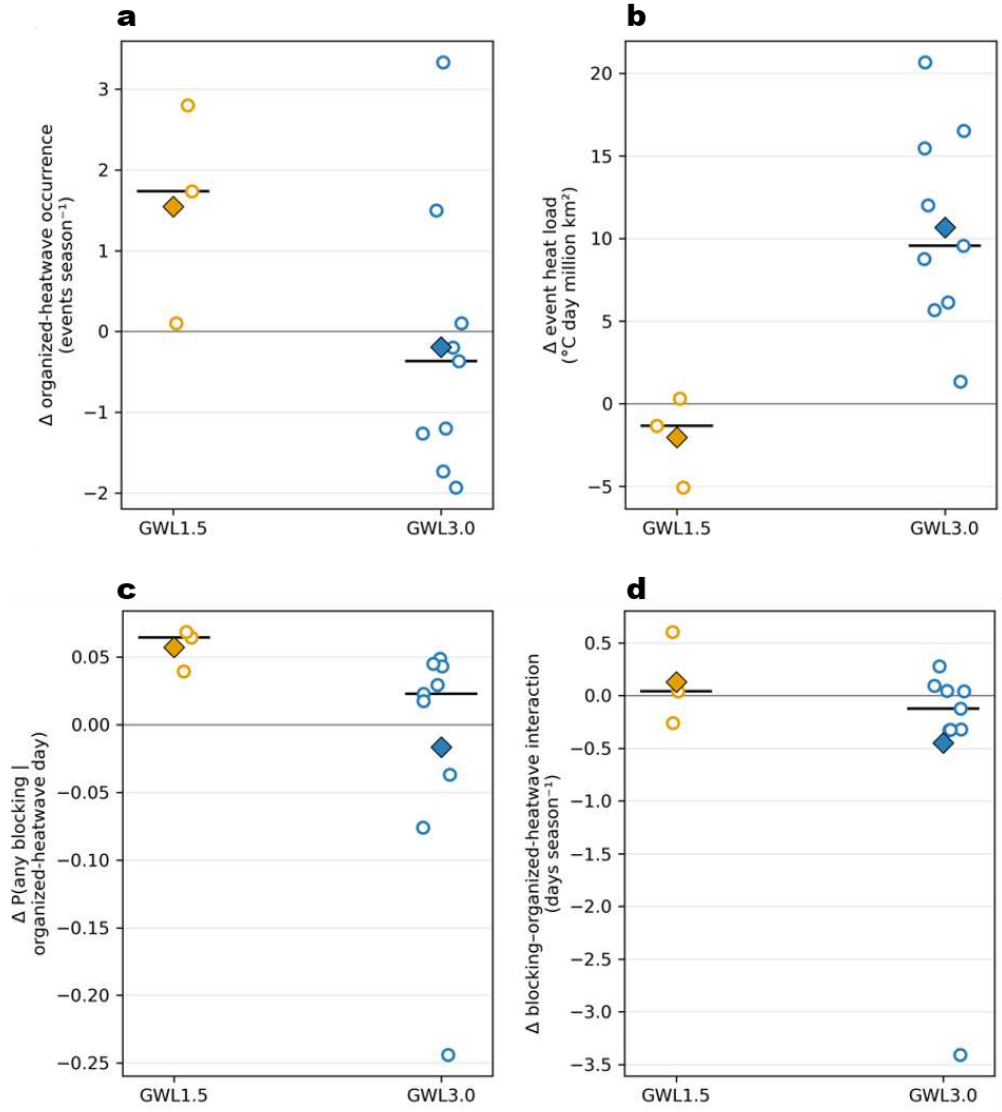

Extended Data Fig. 8. Ensemble-member contrasts in organized-heatwave occurrence, thermal burden and blocking association across two warming states. Future-minus-historical changes in

organized Eurasian heatwaves and their relationship with atmospheric blocking across the available high-resolution Earth system model ensemble members. The two ensembles represent climate states corresponding approximately to GWL 1.5°C and GWL 3.0°C above the pre-industrial baseline, sampled from the available low- and high-warming simulations, respectively. Organized heatwaves are identified independently within each climate state using the period-specific classification framework. **a**, Change in organized-heatwave occurrence rate, expressed as events per MJJAS season. **b**, Change in mean event heat load, calculated by integrating temperature anomaly over event duration and affected area. **c**, Change in the conditional probability that an organized-heatwave day coincides with blocking, P(blocking day | organized-heatwave day). **d**, Change in the blocking–organized-heatwave interaction, defined as the future-minus-historical change in the contrast in organized-heatwave occurrence between strong-blocking-onset and no-blocking-onset conditions. Open circles denote individual ensemble members, diamonds the ensemble means, and horizontal black bars the ensemble medians. Horizontal grey lines indicate zero change. The available ensembles comprise three members at GWL 1.5°C and nine members at GWL 3.0°C and are not paired across warming states. Constituent simulations, forcing pathways and warming-state definitions are described in Methods.

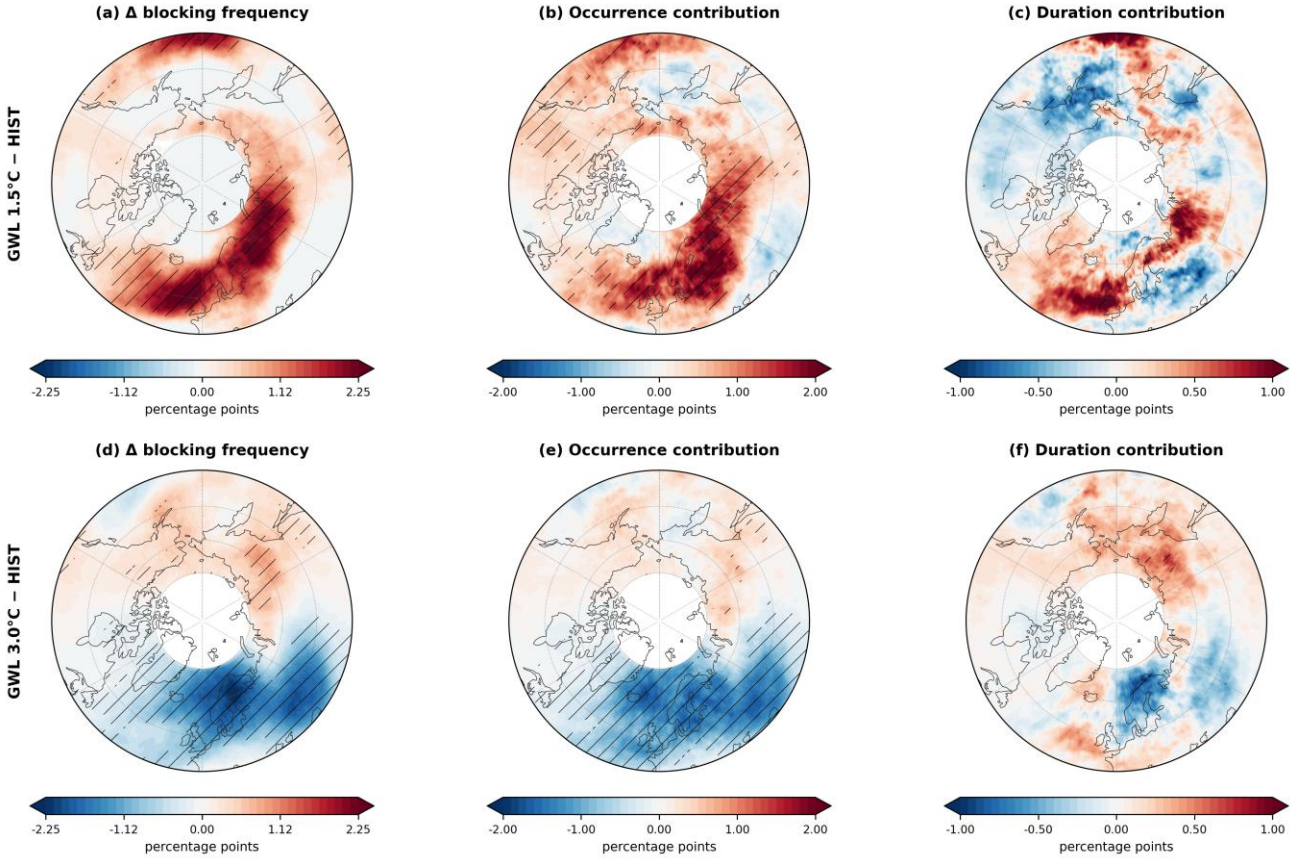

Extended Data Fig. 9. Ensemble-mean changes in warm-season blocking and their occurrence

and residence-duration contributions across two warming states. Ensemble-mean future-minus-historical changes in May–September (MJJAS) blocking frequency and their decomposition for climate states corresponding approximately to GWL 1.5°C and GWL 3.0°C above the pre-industrial baseline. **a–c**, GWL 1.5°C minus HIST; **d–f**, GWL 3.0°C minus HIST. **a,d**, Changes in blocking frequency, defined at each grid cell as the fraction of MJJAS days classified as blocked. **b,e**, Contributions from changes in local blocking-spell occurrence rate. **c,f**, Contributions from changes in mean blocking-spell residence duration. Blocking-frequency changes are separated into occurrence and residence-duration contributions using the two-factor midpoint decomposition described in Methods; the two contributions sum to the total blocking-frequency change. All changes and contributions are expressed in percentage points. Hatching indicates grid cells where the ensemble-mean change differs from zero according to a two-sided Welch's t-test ($p<0.05$) and more than 50% of ensemble members agree with the sign of the ensemble-mean response. The available ensembles comprise three members at GWL 1.5°C and nine members at GWL 3.0°C. Details of the constituent simulations, forcing pathways, ensemble construction and warming-state definitions are provided in Methods.

Supplementary Files

This is a list of supplementary files associated with this preprint. Click to download.

- SI20260906.docx